# Mapping whole-brain projections of anatomically-defined prefrontal neurons using combined 3D convolutional networks

Michael W. Gongwer[1,2,3*], Cassandra B. Klune[1,2*], Alexander S. Enos[1], Rita Chen[1], Drew Friedmann[4] and Laura A. DeNardo[1,#]

Author Affiliations: [1]Department of Physiology, [2]Neuroscience Interdepartmental Program, [3]Medical Scientist Training Program, University of California Los Angeles, [4]Cajal Neuroscience, Seattle, WA

*Denotes equal contribution

[#]Correspondence: Dr. Laura DeNardo, 10833 Le Conte Ave, Center for Health Sciences, David Geffen School of Medicine at UCLA, Los Angeles, CA 90095 ldenardo@ucla.edu

**Abstract** Long-range axonal projections provide the foundation for functional connectivity between brain regions and are critical in the modulation of behavior. Descending projections from medial prefrontal cortex (mPFC) to various target regions regulate critical behavioral functions including decision making, social behavior and mood. While specific mPFC projections have distinct behavioral roles, individual mPFC projection neurons can also innervate multiple target regions. Yet how mPFC projection neurons divide their axons across the brain is poorly understood. In this study, we mapped the axon collaterals of mPFC neurons that project to nucleus accumbens (NAc), ventral tegmental area (VTA), or contralateral mPFC (cmPFC) in mice. We used tissue clearing and light sheet fluorescence microscopy to visualize the 3-D structure of axonal arbors across the intact brain. While machine learning can automate analysis of axons in images of cleared tissue, it is challenging to train a model that generalizes to all axonal structures because the appearance of axons varies by target region. In this study, we present DeepTraCE (Deep learning-based image Tracing with Combined-model Enhancement), a new strategy for axon segmentation and quantification in images of cleared

tissue. DeepTraCE is based on the deep-learning framework TRAILMAP; it achieves highly accurate axon detection by combining multiple machine learning models that are each applied to different brain regions. Using DeepTraCE, we find that cmPFC, NAc, and VTA-projecting mPFC neurons represent largely separable classes with unique axon collaterals in cortical, olfactory, and thalamic regions, respectively.

**Introduction** The medial prefrontal cortex (mPFC) is a vastly interconnected brain region that controls complex cognitive and emotional functions including memory, decision making, social interactions and mood[1–3]. mPFC acts through its axonal projections to exert top-down control, biasing activity in downstream brain regions to promote adaptive responding to the environment[4,5]. Recent studies have linked individual mPFC projections to discrete behavioral functions[6–16]. On the other hand, many mPFC-dependent behaviors are known to involve multiple downstream brain regions[17]. Taken together, these studies suggest that subtypes of mPFC neurons may engage in specific behaviors by controlling small groups of downstream regions. This functional organization may arise from classes of mPFC projection neurons that send branched axon collaterals to specific sets of brain regions. Yet how mPFC neurons divide up their axons across the brain is poorly understood (Figure 1A).

We mapped the brain-wide axonal collaterals of neurons in the prelimbic (PL) subregion of mPFC that project to the contralateral PL (cPL), nucleus accumbens (NAc) or ventral tegmental area (VTA). These projection classes are widely studied from a behavioral perspective, but little is known about their connectivity at the whole-brain level. PL-cPL, PL-NAc and PL-VTA neurons have distinct distributions across cortical layers, distinct genetic profiles, and distinct functions[9,12,18]. PL-cPL connections are important for both hemispheric synchronization and lateralization of mPFC activity; lateralized activity has been associated with anxiety-like behavior[19] and stress responses in rodents[20–22], and psychiatric illness in humans[23]. PL-NAc neurons control reward seeking, social preference, threat avoidance, and strategy

shifting[9,13,24–26]. PL-VTA neurons respond to both positive and negative stimuli and are involved in appetitive conditioning[15,27]. It is important to note that many of these studies used virally-delivered neuronal activators (e.g. opsins[28] or DREADDS[29]) to determine the roles of projection-defined mPFC neurons during behavior[7,9–13]. With this experimental design, activation of axon collaterals can inadvertently influence animal behaviors. Our understanding of how PL-cPL, PL-NAc and PL-VTA neurons control behavior is limited because we lack detailed maps of their axon collaterals.

Traditional studies of axon collaterals have established an important foundation of knowledge but have been limited by low throughput approaches. Anatomical mapping strategies include injecting retrograde tracers into multiple target areas and measuring overlap in source neurons[9,30]. Functional mapping strategies include recording from source neurons while performing multisite antidromic stimulation in target regions[24,31]. While informative, these approaches are biased – users predefine the target areas to investigate – and limited to small numbers of regions. For most anatomical studies, researchers analyze connectivity manually in 2-dimensional (2-D) brain slices, a laborious process in which individual slices are difficult to align to a reference brain. As a result, it is challenging to visualize the 3-D relationships of cells across sections. RNA-sequencing based approaches[32] allow higher throughput examination of collateralization, but the spatial resolution is limited by tissue micro-dissection volumes and analyses are also limited to experimenter-defined sets of regions.

Tissue clearing methods[33,34] combined with light sheet fluorescence microscopy can preserve 3-D circuit architecture in intact tissue without the need to align structures. Advances in computer vision now allow researchers to train classifiers to automatically detect axons in tissue volumes[35,36]. However, classifiers sometimes fail to identify all axons because axon appearance varies across brain regions. Variance in axonal appearance is partly due to the resolution limitations of most light sheet microscopes that are capable of visualizing entire mouse brains in a timely fashion. Axons can appear thick and bright in sparsely innervated brain

regions near the surface of the brain, but thin and indistinct in densely innervated regions deep in the tissue.

To overcome these hurdles, we developed DeepTraCE (Deep-learning based image Tracing with Combined-model Enhancement), a novel strategy for axon segmentation in images of cleared tissue. DeepTraCE builds upon a machine-learning based axon segmentation pipeline called TRAILMAP[36]. After TRAILMAP trains several models to detect axons in 3-D, DeepTraCE combines model outputs, applying different models to different brain regions depending on the appearance of local axons. After segmenting the axons, DeepTraCE registers the brains to a common coordinate framework and quantifies innervation density by brain region.

In the present study, we used DeepTraCE in combination with viral circuit tracing, tissue clearing, and light sheet microscopy to generated unbiased, whole-brain maps of PL-cPL, PL-NAc and PL-VTA axon collaterals. First, we quantitatively compared projection patterns for the three neuronal classes across all brain regions. While each class innervated dozens of brain regions, we identified nearly 30 differentially innervated regions, most of which were located in the cortex, subplate and thalamus. Next, we carefully examined each of those areas, identifying striking topographic, layer-specific and region-specific innervation patterns across the three classes. Finally, we performed unbiased analyses of the collateralization patterns, finding that classes were largely separable based on their collateralization patterns. Overall, PL-cPL and PL-VTA neurons were distinguished by their projections to cortex/subplate and thalamus/hypothalamus/midbrain, respectively. PL-NAc neurons shared collateral targets with both other classes, but also sent unique collaterals to groups of olfactory and limbic areas. Our data support a model in which PL-cPL, PL-NAc and PL-VTA are separable neurons classes that are defined by biased collateral outputs to groups of PL targets and that contain heterogeneity. Indeed, we propose the existence of potential subclasses that can be investigated in future studies.

## Results

We hypothesized that classes of PL projection neuron collateralize to distinct subsets of target regions (Figure 1A). To test this, we used a dual-virus approach to fluorescently label PL-cPL, PL-NAc-, and PL-VTA neurons. In contrast to multi-site retrograde tracer injections, this approach allows us to visualize their entire axonal arbors – including all the collaterals – in an unbiased way. Using light sheet imaging and machine learning analyses, we then quantified innervation density across all brain regions and compared across neuronal types.

### Viral circuit mapping strategy

We first injected an axon-terminal-transducing adeno-associated virus[37] expressing Cre recombinase (AAVrg-hSyn-Cre) into cPL, NAc, or VTA. Next, into PL, we injected AAV expressing Cre-dependent EYFP-tagged Channelrhodopsin-2 (AAV8-hSyn-DIO-ChR2-EYFP), which traffics efficiently to axons (Figure 1B). We examined 2-D brain sections to determine the location of retrogradely labeled cell bodies and get a broad overview of their projection patterns. For each cell type, retrogradely labeled cell bodies had different but partially overlapping locations across PL layers that aligned with previous literature[38]. PL-cPL neurons were preferentially located in layer (L) 2–5a, PL-NAc neurons were distributed across L2–6, and PL-VTA neurons were restricted to L5b (Figure S1A). Axon collaterals from PL-cPL neurons were observed in cortex, striatum, and subplate regions. PL-NAc neurons collateralized broadly, including to the cortex, thalamus, hypothalamus, amygdala, and claustrum. Collaterals of PL-VTA neurons appeared in the thalamus and midbrain (Figure 1B). Overall, PL-cPL, PL-NAc and PL-VTA neurons collateralize extensively to distinct but partially overlapping sets of brain regions.

### DeepTraCE Workflow

To map the brain-wide collateralization patterns in 3D, we used the same viral tracing strategy and visualized axons in cleared intact brains. Using an iDISCO clearing variant, Adipo-Clear[39,40], we immunostained intact brains for GFP and then rendered the tissue transparent. We then imaged the hemispheres ipsilateral to the PL injection on a light sheet fluorescence microscope. We used TRAILMAP[36], a machine learning pipeline that trains a 3D U-net framework to automatically identify axons in cleared tissue (Figure 2A, Figure S2). TRAILMAP provides a pre-trained model that users can fine tune to fit their samples. However, it was challenging to train a model that could sufficiently generalize across the diversity of mPFC axonal structures in all of their target regions; some axons were bright and delineated (e.g. in cortical areas) while others were dense and indistinct (e.g. in the basolateral amygdala and thalamus).

To surmount this hurdle, DeepTraCE combines multiple trained models to optimize axon detection throughout the brain. After importing 3-D image stacks, DeepTraCE fully segments each brain using multiple models, registers each brain to a standard atlas, and generates a new image in which pixel values in each region were extracted from the assigned model. Axons in the resulting images are then thinned to single-pixel width using the TRAILMAP pipeline and the number of axon-containing pixels are quantified for each brain region (Figures 2A).

**Validation of model combination method**

To determine how many models to combine, we examined raw images from the light sheet microscope. Based on our visual inspection, we grouped brain regions into three main bins – ‘delineated, ‘marginally distinguished’, or ‘indistinct’ – depending on the ability to identify the structure of individual PL axons. We used TRAILMAP[36] to train three separate models that we fine-tuned for each set of regions (Figures 2B,C; Figure S2A–C).

To validate the DeepTraCE model assignments, we performed quantitative comparisons of model accuracy in representative brain regions from each category, using human annotations as a reference. Human experts finely traced pixels containing axons in images with clearly

delineated axons and broadly estimated groups of pixels likely to contain axons in images with marginally-distinguished and indistinct axons (Figures S2A–D). We segmented images using each of the three models in addition to the original untuned TRAILMAP model that was trained on serotonergic axons. We then calculated the resulting axonal labeling density with reference to human labels. For reasons described below, common metrics such as F1 Score, precision, and recall do not provide interpretable measures of segmentation accuracy with our method. To validate our pipeline, we instead developed a distinction score based on labeling density in pixels that humans labeled as axon-positive and axon-negative.

In light sheet microscopy of cleared tissue, the size of small fluorescent structures are amplified such that a thin object such as an axon occupies several more pixels in the image than it does in true biological space. As in TRAILMAP, we account for this overrepresentation by thinning segmented axons to a single pixel width. However, because rapid imaging of intact rodent brains requires lower optical resolution, it can be challenging to hand-label axons with single pixel precision. This caveat to whole-brain light sheet microscopy approach prevents the calculation of “true positive” and “true negative” rates based on human annotation. Instead, our distinction score calculates the density of segmented axons in regions that humans estimated as containing axons vs. not containing axons. A higher distinction score indicates better overlap with human labels. When applied to our validation set, Models 1, 2, and 3 produced the highest distinction scores in images containing delineated, marginally-distinguished and indistinct axons, respectively (Figure S2F).

Previous studies used alternative approaches to overcome the limitations of a single-model approach in whole-brain image segmentation. Some excluded deeper, more densely innervated areas from analysis[41]. Others combined probability maps from different segmentation methods by extracting the maximum probability for each pixel[42]. To compare DeepTraCE with these alternative approaches, we calculated the distinction score across all human-annotated images in the validation set using the original untuned TRAILMAP model (originally trained on

serotonin neurons), our best-trained single model, the maximum probability between our three models, the sum of probabilities, and the DeepTraCE combined models. DeepTraCE had the highest distinction score (Figure S2G), indicating that it performed the more accurate axon segmentation from images.

**Whole-brain projection patterns of PL-cPL, PL-NAc and PL-VTA neurons**

We used DeepTraCE to determine the extent to which PL-cPL, PL-NAc and PL-VTA neurons collateralize to other brain regions. We analyzed four brains from each class. After axon segmentation from image volumes and registration to the brain atlas, DeepTraCE quantifies axon innervation by brain region. Examination of thin optical sections revealed widespread collateralization for all three classes. Overall, innervation patterns were consistent with reports of general mPFC projection patterns[30,43,44]; mPFC axons were prominent in cortical association areas, striatum, midline thalamus, claustrum, amygdala, hypothalamus and midbrain but largely absent from hippocampus, sensory thalamus, and relatively sparse in primary sensory areas (Supplemental Video). However, we observed striking differences in the innervation patterns of the three projection classes, particularly in the cortex, olfactory areas, amygdala, thalamus and midbrain (Figure 3A–C; Figure S3–5).

We generated dotograms[45] to visually summarize the inter-class distinctions and observed regions with both quantitative and qualitative differences in innervation. To create the dotogram, we averaged axon density across all samples for a given projection class and then overlaid the samples in brain space. Dot color indicates the neuronal class and dot size corresponds to the averaged axonal density within a voxel (Figure 3D). Compared to PL-VTA neurons, PL-cPL and PL-NAc neurons more densely innervated cortical regions. On the other hand, PL-VTA collaterals preferentially innervated thalamic (TH) and midbrain (MB) regions, a subset of which also received collateral input from PL-NAc neurons. All three subtypes innervated NAc and olfactory tubercle (OT), while PL-NAc neurons were the primary source of

collaterals to piriform cortex (PIR). These patterns were consistent with what we observed in 2D brain sections (Figure 1B), indicating that DeepTraCE accurately captured meaningful class-specific distinctions in collateral targets.

We next quantified regional innervation densities and plotted them as a heatmap. For each brain, we normalized the number of axon-containing pixels in each region to the total number of axon-containing pixels in the brain. We then sorted regions according to their innervation density by projection classes; regions receiving more PL-cPL collaterals are on top and those receiving more PL-VTA collaterals are in the bottom half of the heatmap (Figure 3E). There was relatively little overlap between projection patterns of PL-cPL and PL-VTA neurons. PL-NAc neurons, however, shared several projection targets with both other projection classes. Brain-wide statistical comparisons confirmed the presence of 29 significantly differentially innervated brain regions, the most notable of which were in the cortex, subplate, and thalamus (Figure S6, Table 2, Table 3). We investigated these areas in more detail.

**Collateralization patterns in the cortex and subplate**

PL-cPL, PL-NAc and PL-VTA neurons all sent collaterals to agranular insula (AI), temporal association areas (TEa), the parahippocampal region – including perirhinal (PERI), ectorhinal (ECT) and entorhinal (ENT) cortices – and high order sensory areas (Figure 4A). Within these regions, however, we observed interesting subclass-specific collateralization patterns. Compared to PL-NAc and PL-VTA, PL-cPL neurons had the densest collaterals in the cortex. PL-cPL axon collaterals were most prominent in AI, TEa, ECT, and PERI along with the claustrum (CLA), which is part of the cortical subplate. Many regions were dually innervated by PL-cPL and PL-NAc collaterals, suggesting PL-cPL and PL-NAc populations share common subclasses. Indeed, gustatory (GU), visceral (VISC), ENTl, AIp, and high order visual (VISpl, VISrl) and auditory areas (AUDd, AUDv) received equally dense collateral innervation from PL-cPL and PL-NAc neurons, suggesting there may one or more classes of PL neurons that target

cPL, NAc, and GU, VISC, ENTl, AIp, and high order sensory areas. Compared to both PL-cPL and PL-NAc, PL-VTA neurons sent few collaterals to the cortex, but with some exceptions. PL-VTA collaterals were denser than the other classes in medial orbitofrontal cortex (ORBm). In VISpm and AIv, the density of PL-VTA and PL-NAc collaterals was similar, but lower than PL-cPL collateral density. ORBm, AIv, and VISpm may have privileged communication with PL-VTA neurons (Figure 4A,B, Table 3).

Many PL target regions contain functional gradients. We therefore investigated whether PL axons favor topographic locations in target regions and if there are distinctions between projection classes. We plotted the anterior-posterior distribution of labeled axons within several cortical areas and observed striking subclass-specific topographic trends. PL-NAc collaterals were especially prominent in the posterior piriform cortex (PIR). Compared to PL-cPL PL-NAc, PL-VTA collaterals had a tighter distribution in the anterior portion of AI (Figure 4C). Both PIR and AI are both complex anatomical hubs with distinct functional zones along the A-P axis[46–48]. Preferential innervation by PL projection neurons may underlie some of the functional specializations within these regions.

The neocortex is organized into layers that contain distinct neuronal types with different morphology, physiology, and connectivity[38,49]. Long-range cortico-cortical axons may innervate superficial or deep layers depending on the hierarchical relationship with the target region[38,49]. Compared to sensory and motor cortices, much less is known about the layer organization of long-range mPFC connectivity, especially for specific projection classes. To investigate this, we plotted PL-cPL, PL-NAc and PL-VTA collateral innervation density across layers in cortical target areas (Fig. 4D). In ORB, all classes preferentially targeted superficial layers (L1, L2/3). In AUD, TEa, ECT, and PERI, PL-cPL and PL-NAc collaterals preferentially targeted superficial layers (L1, L2/3) while PL-VTA collaterals targeted the deep layers (L5, L6) (Figure 4D, Table 3). In ENT, axon collaterals were more prominent in deep layers for all 3 classes. These findings suggest that PL-cPL, PL-NAc and PL-VTA may all participate in feedforward or feedback

connectivity depending on the target region. Further, while PL-cPL and PL-NAc collaterals had similar layer-specific innervation patterns in all regions we quantified, PL-VTA collaterals had opposing patterns in some of the regions, suggesting their role in intracortical communication is distinct from the other two classes.

While all projection classes sent collaterals to the amygdalar complex, amygdalar nuclei were differentially innervated. Most notably, the anterior basolateral amygdala (BLAa) was robustly innervated by PL-cPL and PL-NAc neurons, but significantly less so by PL-VTA neurons. Meanwhile, compared to PL-cPL neurons, PL-NAc neurons sent many more collaterals to olfactory amygdalar areas, including anterior cortical amygdalar area (COAa) and piriform amygdalar area (PAA) (Figure 5A–C). As PL-NAc collaterals were also more prominent in posterior PIR compared to the other two classes, PL-NAc neurons may have privileged control over areas dedicated to olfactory processing during cognition and emotional learning.

**Collateralization patterns in the thalamus**

PL projections to the thalamus play a key role in cognition, but whether and how classes of PL neurons divide up their axons across thalamic nuclei remains poorly understood. Compared to the other projection classes, PL-VTA axon collaterals were particularly dense in the thalamus (Figure 1B, Fig. 3). PL-VTA collaterals were particularly notable in the medial (MED) and midline thalamic nuclei (MTN) and the medial and lateral habenula (MHb, LHb). PL-NAc neurons also densely collateralized in MHb, MED and MTN, suggesting PL-VTA and PL-NAc neurons may share subclasses that project to VTA, NAc, MHb, MED and MTN. Interestingly, corticocortical neurons are generally thought not to collateralize to the thalamus[38,49–51]. However, although sparse, we observed PL-cPL collaterals in MED, ILM and MTN with varicosities reminiscent of synaptic release sites (Figure 5D,E). These collaterals may be a unique feature of mPFC neurons that can be further investigated with functional studies.

We also analyzed the topographic innervation of some of the most densely innervated thalamic nuclei. PL axons favored anterior portions of MTN, posterior portions of LHb and were relatively evenly distributed across the MED nuclei (Figure 5F). The topographic organization was similar across subclasses, suggesting the location within PL, rather than projection class, was the major determinant of axon location in thalamic regions.

**Unbiased assessment of brain-wide collaterals**

Because PL-cPL, PL-NAc and PL-VTA projection neurons all collateralize broadly, we wondered if these neuronal classes could be separated based on their whole-brain projection patterns. To unbiasedly assess differences between their whole-brain projection patterns, we implemented two dimensionality reduction techniques. We first performed hierarchical clustering, in which euclidean distance between individual brains based on axonal density in each subregion is marked by a higher branch point on the graph. PL-VTA neurons formed a distinct cluster, while PL-NAc and PL-cPL collaterals formed largely distinct but partially overlapping clusters (Figure 6A). This aligns with our observation that the projection patterns of PL-NAc neurons shared more overlap with PL-cPL than PL-VTA neurons (Fig. 3).

We used principal component analysis to assess differences in whole-brain projection patterns for each cell type. We plotted the location of each brain along the axes of the first two principal components, which account for 41.83% and 16.18% of the variance in the data, respectively. We found that that PL-cPL and PL-VTA projection classes could be clearly separated along the first principal component. PL-NAc brains were positioned in between, with some overlap with PL-cPL brains (Figure 6B). To assess which distinguished the classes, we plotted the weights of each brain region in contribution to the first principal component. Positively weighted regions generally had the most innervation from PL-cPL collaterals including TEa, PERI, and ECT, and negatively weighted regions were those with most innervation from PL-VTA collaterals, including MTN and midbrain areas (Figure 6C). Together, these data

suggest that PL-cPL, PL-NAc and PL-VTA neurons represent mostly separable classes, distinguished in large part by their collaterals to TEa/PERI/ECT, olfactory and limbic areas, and thalamus and midbrain, respectively.

We next assessed the existence of potential connectivity motifs that represent groups of regions that are highly co-innervated by PL projection neurons. Because PL-cPL, PL-NAc and PL-VTA projection classes likely have some overlap, we performed this analysis on our entire dataset (n=12 brains total, n=4 from each class). We calculated the Pearson R correlation between axonal density for all pairs of brain regions. A higher R value represents increased likelihood that two regions share PL collaterals. These R values were plotted on a heatmap and sorted according to the Allen Brain Atlas (Figure 6D). Most cortical regions were highly correlated with other cortical regions, parahippocampal regions, and subplate, but there were some interesting exceptions. ORB cortex was highly correlated with olfactory areas including taenia tecta (TT), dorsal peduncular area, and nucleus of the lateral olfactory tract (NLOT), striatal regions including substantia innominata (SI) and magnocellular nucleus (MA). Since PL-VTA neurons preferentially innervated ORBm (Figure 4), they are a likely source of these shared collaterals. PIR was correlated with a distinct set of regions including COA, PAA, PPA, and BLA. Given the preferential innervation of PL-NAc collaterals in these regions (Figure 4,5), they are a likely source. These findings suggest the existence of two neuronal PL subclasses with biased output connectivity: one that projects to VTA/ORB/TT/NLOT/SI/MA and another to NAc/PIR/COA/PAA/PPA/BLA.

To further explore the existence of potential PL subclasses, we generated a network diagram for strongly correlated region pairs ($R>0.85$ and $p<0.05$), with brain regions colored by their weight in the first principal component (Figure 6E). This yielded two large networks of prefrontal collateralization, along with small ‘networks’ of paired regions. One large network comprised cortical and subplate regions that were densely innervated by PL-cPL and, to some extent, PL-NAc collaterals. The other comprised regions in the thalamus, hypothalamus,

midbrain and hindbrain that are densely innervated by PL-VTA and, in some cases, by PL-NAc collaterals. Each larger network contained one tightly interconnected subnetwork. Innervation density was tightly correlated in a subset of PL-cPL collateral sites – ENTl, ECT, PERI, TEa, AUDp, AUDv, VIS, VISrl, GU, AIp, MOp, SSs, CLA, and BLAa – suggesting these regions are co-innervated by a subclass of PL-cPL neurons. The other subnetwork represents another likely PL-VTA subclass that projects to five thalamic nuclei (RT, VENT, APN, SPF, TH) and the zona incerta (ZI), a hypothalamic region (Figure 6E). Overall, our data support a biased connectivity model for PL (Figure 1) in which PL-cPL, PL-NAc and PL-VTA are largely separable populations with some overlap. Each class contains some unique subclasses defined by their projections to small groups of downstream regions. PL-NAc appears to be the most heterogenous, with many shared targets with the other classes.

## Discussion

We defined the brain-wide collateral projections of PL-cPL, PL-NAc, and PL-VTA neurons. These neurons have distinct, important behavioral functions, but their global connectivity patterns remained unknown. Our data indicate that PL-cPL, PL-NAc, and PL-VTA neurons are separable classes of projection neurons, potentially with distinct subclasses embedded within them. PL-cPL neurons are distinguished by their collaterals to cortical association areas including AI, TEa, PERI, ECT, CLA, ENT and high order visual and auditory areas. We also identified unexpected PL-cPL collaterals in the thalamus. PL-VTA neurons collateralized to specific regions in the thalamus –especially MTN, MED, and LHb – along with hypothalamus and midbrain. PL-NAc neurons collateralized more broadly than the other classes, including to many of the regions targeted by PL-cPL and PL-VTA neurons. While PL-NAc neurons shared targets with both PL-cPL and PL-VTA neurons, prominent collaterals to posterior PIR, COA, and PAA distinguished PL-NAc from the other classes (Figure 7A,B).

We quantified the brain wide collateralization patterns of these neurons using DeepTraCE, a method we developed. DeepTraCE builds upon TRAILMAP by combining multiple deep learning networks to accurately identify axons, which can differ in appearance across brain regions. Variance in axonal appearance across the brain can arise due to differences in axon morphology and density, due to differences in light penetration throughout the tissue, and due to the resolution of the light sheet optics capable of imaging an intact mouse brain in a few hours. By combining different models that are uniquely suited to axons with distinct visual qualities, DeepTraCE allowed us to quantify the brain-wide axonal projection patterns more accurately than previous methods (Figure S2D).

Our viral approach bulk labels many neurons at once, so the observed output organization may represent the compound projections patterns of multiple subclasses within a projection class. Indeed, recent single neuron reconstructions of prefrontal neurons indicate that individual neurons project to approximately 5 brain regions[52]. Subclasses may be defined by multiple factors including their layer of origin and transcriptional profile. PL-VTA and PL-cPL were the most separable projection classes of the three and, consistent with previous studies, we see that PL-VTA neurons reside exclusively in L5b,[5330] while PL-cPL neurons reside mostly in L2/3 and 5a[54,55] (Figure S1A). PL-NAc, which collateralized most broadly, spanned layers 2-6. Consistent with this, cortico-striatal neurons in mPFC are more numerous than in other cortical areas and are distributed more evenly across layers[38]. Layer of origin may therefore explain some of the diversity in PL-NAc collaterals[44].

Transcriptomic heterogeneity has been observed within individual classes of prefrontal projection neurons[18], suggesting they contain genetically-defined subpopulations. Cre driver lines and transcriptome sequencing of projection-defined neurons further indicate that genetically defined subclasses may exist that project to small groups of target regions[56]. For example, Colgat2+ neurons in mPFC project to NAc, dorsal striatum (DS), ZI, and BLA[55]. Since Colgat2+ axons do not innervate all targets of PL-NAc collaterals that we observed, Colgat2

may indicate a subset of PL-NAc neurons that collateralize to a specific subsets of PL-NAc target regions. A recent sequencing study identified a set of genes including *Npr3, Otof, Syt6* and *Tshz2* that are differentially expressed in classes mPFC projection neurons and may define subclasses that project to combinations of BLA, DS, HY, NAc PAG and cPFC[18]. Our data support a model in which PL projection classes are heterogeneous. Embedded subclasses may influence behavior via simultaneous control of ~5–10 brain regions (Figure 7C).

PL-VTA neurons are distinguished in part by their dense collateral innervation of thalamic nuclei including MED, MTN, SPA, PP, MHb and LHb. Separate studies found that mPFC projections to VTA and thalamus both encode learned information about predictive cues during adaptive decision making. While mPFC-VTA neurons can compare predictions with outcomes encoded by VTA dopamine neurons[57], mPFC neurons projecting to the paraventricular thalamus, part of MTN, can bias decision making towards predicting negative outcomes[58]. Another PL-VTA collateral site, MD thalamus, also plays a key role in decision making[59]. PL-VTA neurons reside in L5b. In contrast to L6 projections, which modulate thalamic activity, L5 PL projections strongly activate thalamic neurons[53]. PL-VTA neurons may therefore influence cognition by exerting powerful, simultaneous top-down control over a subset of thalamic areas.

During social interactions, NAc, BLA, COA, TEA, PERI and ECT are activated in the mouse brain[17]. We found that PL-NAc collaterals innervated all of these regions and previous studies showed that PL-NAc and PL-BLA both directly regulate social behavior[9,60]. Therefore, individual PL neurons may send divergent outputs to this set of regions to control social behaviors.

fMRI studies in both humans and rodents indicate that prefrontal top-down control is disrupted in numerous neuropsychiatric disorders[61–64]. For instance, disrupted prefrontal long-range communication and decreased interhemispheric functional connectivity are core features of pathophysiology in autism spectrum disorder (ASD)[65–67]. We find that PL-cPL and PL-NAc,

collateralize to several key regions disrupted in ASD including TEa, ECT, PERI, ENTl, BLA, AI, and NAc[68]. Dysfunction in a subclass of prefrontal neurons collateralizing to these regions may contribute to ASD pathogenesis.

Here, we present comprehensive projection maps of three PL projection classes as well as a new analysis pipeline that allows more accurate axon segmentation from brain volumes. However, it is important to note some limitations of our study. First, DeepTraCE is not completely automated. It requires an initial time investment during which users assign machine learning models to brain regions. Also, our viral labeling method does not distinguish between axon terminals and axons of passage. Although we cannot claim that axons make direct synaptic connections in target areas, many of the putative connections we observed have been validated with electrophysiology[44,69,70] or rabies trans-synaptic tracing[47,71–74]. These caveats are balanced by the ability to analyze the brain-wide projection patterns of defined neuronal classes in a highly accurate, high throughput and unbiased way. Our data illuminate new organizational properties of PL circuits. We propose that PL-cPL, PL-NAc and PL-VTA projection neurons represent separable classes but are also heterogeneous populations. Each likely consists of multiple neuronal subclasses that project to 5–10 brain regions, with PL-NAc being the most heterogeneous of the three (Figure 7C). The many collaterals we observed are important considerations for circuit dissection studies that use opto- or chemogenetics to activate projection-defined neurons during behavior. Our observations can inform the design of new studies that determine how mPFC controls behavior via multi-region influence.

## Methods

### Animals

Female and male C57B16/J mice (JAX Stock No. 000664) were group housed (2–5 per cage) and kept on a 12 hr light cycle. All animal procedures followed animal care guidelines approved by the University of California, Los Angeles Chancellor's Animal Research Committee.

**Surgery**

Mice were induced in 5% isoflurane in oxygen until loss of righting reflex and transferred to a stereotaxic apparatus where they were maintained under 2% isoflurane in oxygen. Mice were warmed with a circulating water heating pad throughout surgery and eye gel was applied to the animal's eyes. The mouse's head was shaved and prepped with three scrubs of alternating betadine and then 70% ethanol. Following a small skin incision, a dental drill was used to drill through the skulls above the injection targets. A syringe pump (Kopf, 693A) with a hamilton syringe was used for injections. Injections were delivered at a rate 75nL/min and the syringe was left in the brain for 7 minutes following injection. For collateralization mapping, 300uL of AAVrg-Ef1a-mCherry-IRES-Cre-WPRE (Addgene 55632-AAVrg, $1.7x10^{13}$ vg/mL) was injected unilaterally into either left NAc (AP: 1.3, ML: -1.0, DV: 4.7), left VTA (AP: -3.3, ML: 0.4, DV: -4.5), or right PL (AP: 1.8, ML: -0.5, DV: -2.3). 200uL of AAV8-hSyn-DIO-hCHR2(H134R)-EYFP-WPRE ($1.7x10^{13}$ vg/mL) was then injected into left PL (AP: 1.8, ML: -0.4, DV: -2.3). To control for Cre-independent expression of EYFP, control mice received a single injection of 200uL of AAV8-hSyn-DIO-hCHR2(H134R)-EYFP-WPRE into left PL. For topographical mapping of the origin of each projection type, mice were injected with 300uL of cholera toxin subunit B (ThermoFisher, C34775, C34776, C34778) of Fluorogold (SCBT, C223769) at the same coordinates for cPL, NAc and VTA listed above. For pain management mice received 5mg/kg carprofen diluted in 0.9% saline subcutaneously. Mice received one injection during surgery and daily injections for two days following surgery. Samples with mistargeted injection sites were excluded from analysis. Samples with obviously poor antibody penetration or distribution following tissue clearing were also excluded.

**Brain Slice Histology and Immunostaining** Mice were transcardially perfused with phosphate-buffered saline (PBS) followed by 4% paraformaldehyde (PFA) in PBS. Brains were

dissected, post-fixed in 4% PFA for 12–24h and placed in 30% sucrose for 24–48 hours. They were then embedded in Optimum Cutting Temperature (OCT, Tissue Tek) and stored at -80°C until sectioning. 60um floating sections were collected into PBS. Sections were washed 3x10min in PBS and then blocked in 0.3% PBST containing 10% normal donkey serum (JacksonImmunoresearch, 17-000-121) for 2h. Sections were then stained with chicken anti-GFP (AVES 1020 at 1:2000) in 0.3% PBST containing 3% donkey serum overnight at 4°C. The following day, sections were washed 3x5min in PBS and then stained with secondary antibody (JacksonImmunoresearch Cy2 donkey anti-chicken IgG(H+L) 703-225-155, 1:1000) in 0.3% PBST containing 5% donkey serum for 2 hours at room temperature. Sections were then washed 5 min with PBS, 15 min with PBS+DAPI (Thermofisher Scientific, D1306, 1:4000), and then 5 min with PBS. Sections were mounted on glass slides using FluoroMount-G (ThermoFisher, 00-4958-02) and then imaged at 10x with a Leica slide scanning microscope (VT1200S).

**Brain Clearing** Mouse brains were collected and processed based on the published Adipo-Clear protocol[39] with slight modifications. Mice were perfused intracardially with 20mL of PBS (Gibco) followed by 4% paraformaldehyde (PFA, Electron Microscopy Sciences) on ice. Brains were hemisected approximately 1mm past midline and postfixed overnight in 4% PFA at 4°C. The following day, samples were dehydrated with a gradient of methanol (MeOH, Fisher Scientific):B1n buffer (1:1,000 Triton X-100, 2% w/v glycine, 1:10,000 NaOH 10N, 0.02% sodium azide) for 1 hour for each step (20%, 40%, 60%, 80%) on a nutator (VWR). Samples were then washed with 100% MeOH 2x for 1hr each and then incubated in a 2:1 dicholoromethane (DCM):MeOH solution overnight. The following day, two washes of 1hr in 100% DCM were performed followed by three washes of 100% MeOH for 30min, 45min then 1hr. Samples were bleached for 4 hours in 5:1 H2O2/MeOH buffer. A cascade of MeOH/B1n washes (80%, 60%, 40%, 20%) for 30min each rehydrated the samples followed by a 1h wash

in B1n buffer. 5%DMSO/0.3M Glycine/PTxWH permeabilized tissue for one hour and then again for 2h with fresh solution. Samples were washed with PTxwH for 30min and then incubated in fresh PTxwH overnight. The following day two more PTxwH washes lasted 1h then 2h. Samples were incubated in primary GFP antibody (AVES Labs GFP 1020) at 1:2000 in PTxwH shaking at 37°C for 11, washed in PTxwH 2x1h and then 2x2h, then for two days with at least one PTxwH change per day while shaken at 37°C. Samples were then incubated in secondary antibody (AlexaFluor 647, ThermoFisher Scientific) for 8 days shaken at 37°C. Samples were washed in PTxwH 2x1h, then 2x2h, then 2 days with at least one PTxwH change per day while shaken at 37°C. Samples were then washed in 1x PBS twice 1x1hr, 2x2hr and then overnight. To dehydrate samples, a gradient of washes in MeOH:H2O (20%, 40%, 60% and 80%) were conducted for 30min each, followed by 3x100% MeOH for 30min, 1h, then 1.5h. Samples were incubated overnight in 2:1 DCM:MeOH on a nutator. The next day, samples were washed in 100% DCM 2x1h each. Samples were then cleared in 100% DBE. DBE was changed after 4h. Samples were stored in DBE in a dark place at room temperature. Imaging took place at least 24h after clearing.

**Whole Brain Imaging** Brain samples were imaged on a light-sheet microscope (Ultramicroscope II, LaVision Biotec) equipped with a sCMOS camera (Andor Neo) and a 2x/0.5 NA objective lens (MVPLAPO 2x) equipped with a 6 mm working distance dipping cap. Image stacks were acquired at 0.8x optical zoom using Imspector Microscope v285 controller software. We imaged using 488-nm (laser power 20%) and 640-nm (laser power 50%) lasers. The samples were scanned with a step-size of 3 µm using the continuous light-sheet scanning method with the included contrast adaptive algorithm for the 640-nm channel (20 acquisitions per plane), and without horizontal scanning for the 488-nm channel.

**Model Training** Light sheet images of fluorescently labeled axons were segmented using the 3D U-net based machine learning pipeline TRAILMAP (Friedmann et al., 2020). We trained new models for segmentation of cortical axons using inference learning as described in the TRAILMAP pipeline (https://github.com/AlbertPun/TRAILMAP). Briefly, 120x120 pixel stacks of 100 images were selected for training, and axons and artifacts (pixels that could be mistakenly interpreted as axons) were hand-labeled in 3 or 4 images from each stack. 1-pixel-wide edges of axons were labeled using python to be given less weight in training of the 3D convolutional network, which accounts for slight variability in human annotation patterns.

Models 1, 2, and 3 were designed for axon segmentation in regions with delineated, marginally distinguished, and indistinct axons, respectively. Beginning with the published TRAILMAP model weights, trainings were iteratively performed. Model 2 was trained first for 7 sessions and represents our best-trained single model for use across the entire brain. From this, Model 1 for use in superficial regions was trained for 2 sessions and Model 3 was trained for 4 sessions for use in deep regions.

Each training session used between 6 and 20 hand-labeled image stacks, of which approximately 10-20% were set aside for use in model validation. Training was performed using between 20 and 120 steps per epoch and between 5 and 20 epochs per session. The best model from each session was selected by plotting loss in validation data across epoch, which was minimized to prevent overtraining. The weaknesses of the best model from each session were assessed to guide selection of training data for the next session. Sessions were continued until all visible axons in the desired regions were reliably detected by the model.

**Model Validation** We validated our analysis pipeline including image segmentation, scaling and axon thinning by selecting 120x120 pixel stacks of 100 images from regions assigned to the ‘delineated’, ‘moderately distinguished’, and ‘indistinct’ groups in brains that were not included in initial training or validation data sets. Two human experts annotated 2–4 images from each

stack, marking pixels likely to contain axons. In stacks with difficult-to-distinguish axons, such as deep regions, experts used larger brush strokes to label broader groups of pixels likely to contain axons (Figure S2D). One-pixel edges were then added to human annotations in python.

The raw image stacks were segmented as explained below. In brief, each stack was segmented with Models 1, 2 and 3 using TRAILMAP and scaled in ImageJ to a 10um space. Scaled images were skeletonized in python at 8 different thresholds for binarization, combined in MATLAB, and pixel values were adjusted in ImageJ. Using the same quantification threshold as used in all analyses (number of skeletonized pixels with intensity above 64 divided by total number of pixels in the region), labeling density was calculated in human-annotated “axon-positive” pixels (LP) and “axon-negative” pixels (LN), excluding edges to account for slight variability in human labels. Distinction score was calculated from these values as (LP-LN)/LN+(1-LP). While direct true/false positive and true/false negative rates cannot be calculated due to the axon thinning process, which reduces the number of labeled pixels, LP correlates with the true positive rate, LN correlates with the false positive rate, and 1-LP correlates with the false negative rate. Thus, LP-LN in the numerator will increase distinction score when better separation is obtained between true and false positives, and LN and 1-LP in the denominator will decrease the distinction score if there is a higher rate of false positives or false negatives.

Alternate model combination methods were performed in FIJI. Maximum probability projections between all models were calculated by generating images with maximum pixel values across all models for each cube then processing the cubes for validation as above. Summation of probability maps between models was calculated by adding probability calculated by each model, then dividing by 3 prior to processing the cubes for validation as above. Distinction scores from alternate approaches were compared using repeated measures one-way ANOVA with Dunnett’s multiple comparisons test, comparing individual model selection

(DeepTraCE) with each other method. Statistical comparisons of distinguishment scores were performed using GraphPad PRISM.

**DeepTraCE Analysis Pipeline**

*Image Segmentation & Registration*

Whole-brain image stacks from the 640nm channel from each brain were segmented three times in TRAILMAP, once each using models 1, 2, and 3. Following segmentation, the 488nm autofluorescence channel and axon segmentations from each model were converted to 8-bit and scaled to 10um resolution in FIJI with scaling values of 0.40625 in the x and y directions and 0.3 in the z direction using a bilinear interpolation algorithm. To improve image registration, each scaled 488nm image was manually rotated in the x, y, and z planes using the TransformJ ImageJ plugin (https://imagescience.org/meijering/software/transformj/) such that the midline blood vessels visible were all visible in the same z plane. The same manual rotation parameters were then applied to the three scaled model segmentation images from the corresponding brain.

The scaled and manually rotated 488nm autofluorescence channel was registered using elastix to the Gubra Lab LSFM atlas average template, which has annotations based on the Allen CCF[75–77]. The same transformation was applied to the scaled and manually rotated model segmentations using transformix. Image registration quality was manually verified by overlaying the atlas image and the registered 488nm channels in ImageJ. Following segmentation and registration of each model, the transformix images were converted to 8-bit .tif format in ImageJ. When combining multiple probability maps, it is important that minimum and maximum pixel values are comparable between images. Model 1 produced slightly lower maximum probability values compared to the other two models. We corrected for this by brightening segmentations from Model 1 by 34% to match pixel values obtained by the other models prior to combination and thinning.

*Model Combination & Thinning*

Converted segmentations from the three models were then combined by generating a new image in which pixel values in each region were extracted from the model with best performance in that region (Figure 2B). The same regional model assignments for combination were used for all brains in the data set and are provided in Table 2. Following model combination, axon segmentations were thinned (or 'skeletonized') as described in the TRAILMAP pipeline[36]. In brief, images were binarized at 8 different thresholds from 20 to 90% of the maximum intensity value using python. Skeletons were combined in MATLAB by summing values from each skeleton. Small objects unlikely to be axons were removed by calculating connected components within the combined skeleton and removing objects less than 90 voxels in size. Combined skeletons with small objects removed were optimized for visualization and quantification using an ImageJ macro that multiplied each pixel value by 17.

*Axon Quantification*

Regional axon innervation was quantified in MATLAB (Mathworks) by counting the number of skeletonized pixels in each brain region above a threshold (64), then dividing this pixel count by the total number of pixels in a region. This regional pixel count was then divided by the total number of labeled pixels across the brain to normalize for differences in total fluorescence and viral expression. Regions were defined by a collapsed version of the LSFM atlas in which maximum granularity was balanced with the need to account for slight differences in registration which would lead to inaccurate quantification of small brain regions. This atlas was cropped on the anterior and posterior ends to match the amount of tissue visible in our data. Fiber tracts, ventricular systems, cerebellum, and olfactory bulb were excluded from analysis.

All statistical comparisons were performed in MATLAB and GraphPad Prism v9. For comparison of regional axon labeling between cell types, Two-way ANOVA with Tukey's

multiple comparison correction was performed on all brain regions. Anterior-posterior axon distributions within regions were calculated in MATLAB by binning the whole-brain image into 100um voxels and calculating the percentage of segmented pixels within each voxel. Voxels falling within a given region were summed across the medial-lateral and dorsal-ventral axis and normalized for total fluorescence as above. The averaged summation of axon counts from a given cell type was then averaged and plotted along with the standard error of the mean.

*Axon Visualization*

To visualize axons as shown in Figures 2, 4, and 5, Z-projections of raw light sheet data were created in FIJI by scaling images to a 4.0625um space, virtually reslicing images in the coronal plane, and performing maximum intensity z-projections of 100um depth followed by local contrast enhancement. Axon segmentations were created by overlaying skeletonized and registered axon segmentations from each sample of a cell type in a slightly different color and virtually reslicing in the coronal plane. 3D projections were created in Imaris using a representative sample from each cell type. Dotogram overlays (Figure 3) were created using MATLAB. Images were binned into 100um voxels and the percentage of segmented pixels within each voxel was calculated. Area of visible dot in the overlay corresponds with the averaged labeling intensity within a voxel across a cell type. Outer dots represent the cell type with the highest labeling intensity within that voxel.

*Computational Analyses*

Hierarchical clustering of regional axon quantifications was performed as described in Kebschull et al., 2020[42]. Principal component analysis and network analyses were performed in MATLAB. For network analysis, Pearson R correlations were calculated between quantified axons in each brain region and each other brain region to generate a heatmap as shown in Figure 4D. Samples from all labeled cell types were combined for this analysis, and regions with average

labeling density below 0.01 across all cell types were excluded from correlational analysis. Regional correlations with a p value less than 0.05 and an R value greater than 0.85 were plotted as a network diagram. Regions in this network diagram were color coded by their weight within the first principal component from PCA.

## CODE AVAILABILITY

Code, instructions and sample data available at https://github.com/DeNardoLab/DeepTraCE


## ACKNOWLEDGEMENTS

We thank Justus Kebschull and Xiaoyin Chen for helpful comments on the manuscript. This work was funded by an NIH K01MH116264 (L.A.D.), a Whitehall Foundation Research Grant (L.A.D), a Klingenstein-Simons Foundation Grant (L.A.D.), a NARSAD Young Investigator Award (L.A.D.), a Fay/Frank Seed Grant (L.A.D.), an NSERC Postgraduate Fellowship (C.B.K.), and UCLA Medical Scientist Training Program (M.W.G.)


## AUTHOR CONTRIBUTIONS

C.B.K, M.W.G. and L.A.D designed the research; C.B.K. performed the stereotaxic AAV injections and histology; C.B.K. and M.W.G. performed imaging and data analysis; D.F. and M.W.G. wrote DeepTraCE code; R.C. and A.S.E. performed image analysis, C.B.K, M.W.G. and L.A.D. wrote the manuscript.

## DECLARATION OF INTERESTS

None to declare.

## REFERENCES

1. Euston, D. R., Gruber, A. J. & McNaughton, B. L. The Role of Medial Prefrontal Cortex in Memory and Decision Making. *Neuron* **76**, 1057–1070 (2012).

2. Giustino, T. F. & Maren, S. The Role of the Medial Prefrontal Cortex in the Conditioning and Extinction of Fear. *Front. Behav. Neurosci.* **9**, 1–20 (2015).

3. Klune, C. B., Jin, B. & DeNardo, L. A. Linking mPFC circuit maturation to the developmental regulation of emotional memory and cognitive flexibility. *Elife* **10**, 1–33 (2021).

4. Matsuzaki, M. *et al.* Dendritic spine geometry is critical for AMPA receptor expression in hippocampal CA1 pyramidal neurons. *Nat. Neurosci.* **4**, 1086–1092 (2001).

5. Jayachandran, M. *et al.* Prefrontal Pathways Provide Top-Down Control of Memory for Sequences of Events. *Cell Rep.* **28**, 640-654.e6 (2019).

6. DeNardo, L. A., Berns, D. S., Deloach, K. & Luo, L. Connectivity of mouse somatosensory and prefrontal cortex examined with trans-synaptic tracing. *Nat. Neurosci.* **18**, 1687–1697 (2015).

7. Otis, J. M. *et al.* Prefrontal cortex output circuits guide reward seeking through divergent cue encoding. *Nature* **543**, 103–107 (2017).

8. Siciliano, C. A. *et al.* A cortical-brainstem circuit predicts and governs compulsive alcohol drinking. *Science.* (2019) doi:10.1126/science.aay1186.

9. Murugan, M. *et al.* Combined Social and Spatial Coding in a Descending Projection from the Prefrontal Cortex. *Cell* **171**, 1663-1677.e16 (2017).

10. Vander Weele, C. M. *et al.* Dopamine enhances signal-to-noise ratio in cortical-brainstem encoding of aversive stimuli. *Nature* **563**, 397–401 (2018).

11. Warden, M. R. *et al.* A prefrontal cortex-brainstem neuronal projection that controls response to behavioural challenge. *Nature* (2012) doi:10.1038/nature11617.

12. Kim, C. K. *et al.* Molecular and Circuit-Dynamical Identification of Top-Down Neural Mechanisms for Restraint of Reward Seeking. *Cell* (2017) doi:10.1016/j.cell.2017.07.020.

13. Diehl, M. M. *et al.* Divergent projections of the prelimbic cortex bidirectionally regulate active avoidance. *Elife* **9**, 1–13 (2020).

14. Riga, D. *et al.* Optogenetic dissection of medial prefrontal cortex circuitry. *Frontiers in Systems Neuroscience* (2014) doi:10.3389/fnsys.2014.00230.

15. Ye, L. *et al.* Wiring and Molecular Features of Prefrontal Ensembles Representing Distinct Experiences. *Cell* (2016) doi:10.1016/j.cell.2016.05.010.

16. Mathis, V. P., Williams, M., Fillinger, C. & Kenny, P. J. Networks of habenula-projecting cortical neurons regulate cocaine seeking. *Sci. Adv.* **7**, (2021).

17. Kim, Y. *et al.* Mapping Social Behavior-Induced Brain Activation at Cellular Resolution in the Mouse. *Cell Rep.* **10**, 292–305 (2015).

18. Lui, J. H. *et al.* Differential encoding in prefrontal cortex projection neuron classes across cognitive tasks. *Cell* **184**, 489-506.e26 (2021).

19. Costa, N. S., Vicente, M. A., Cipriano, A. C., Miguel, T. T. & Nunes-de-Souza, R. L. Functional lateralization of the medial prefrontal cortex in the modulation of anxiety in mice: Left or right? *Neuropharmacology* **108**, 82–90 (2016).

20. Stevenson, C. W., Halliday, D. M., Marsden, C. A. & Mason, R. Early life programming of hemispheric lateralization and synchronization in the adult medial prefrontal cortex. *Neuroscience* **155**, 852–863 (2008).

21. Sullivan, R. M. & Gratton, A. Lateralized effects of medial prefrontal cortex lesions on neuroendocrine and autonomic stress responses in rats. *J. Neurosci.* **19**, 2834–2840 (1999).

22. Lee, E. *et al.* Left brain cortical activity modulates stress effects on social behavior. *Sci. Rep.* **5**, 13342 (2015).

23. Grimm, S. *et al.* Imbalance between left and right dorsolateral prefrontal cortex in major depression is linked to negative emotional judgment: an fMRI study in severe major depressive disorder. *Biol. Psychiatry* **63**, 369–376 (2008).

24. Ishikawa, A., Ambroggi, F., Nicola, S. M. & Fields, H. L. Dorsomedial Prefrontal Cortex Contribution to Behavioral and Nucleus Accumbens Neuronal Responses to Incentive Cues. *J. Neurosci.* **28**, 5088 LP – 5098 (2008).

25. Domingo-Rodriguez, L. *et al.* A specific prelimbic-nucleus accumbens pathway controls resilience versus vulnerability to food addiction. *Nat. Commun.* **11**, 782 (2020).

26. Cui, Q. *et al.* Dopamine receptors mediate strategy abandoning via modulation of a specific prelimbic cortex–nucleus accumbens pathway in mice. *Proc. Natl. Acad. Sci.* **115**, E4890 LP-E4899 (2018).

27. Parker, J. G., Beutler, L. R. & Palmiter, R. D. The contribution of NMDA receptor signaling in the corticobasal ganglia reward network to appetitive Pavlovian learning. *J. Neurosci.* **31**, 11362–11369 (2011).

28. Zhang, F. *et al.* The microbial opsin family of optogenetic tools. *Cell* (2011) doi:10.1016/j.cell.2011.12.004.

29. Roth, B. L. DREADDs for Neuroscientists. *Neuron* (2016) doi:10.1016/j.neuron.2016.01.040.

30. Gabbott, P. L. A., Warner, T. A., Jays, P. R. L., Salway, P. & Busby, S. J. Prefrontal Cortex in the Rat□: Projections to Subcortical Autonomic , Motor , and Limbic Centers. *J. Comp. Neurol.* **177**, 145–177 (2005).

31. Ishikawa, A. & Nakamura, S. Ventral hippocampal neurons project axons simultaneously to the medial prefrontal cortex and amygdala in the rat. *J. Neurophysiol.* **96**, 2134–2138 (2006).

32. Kebschull, J. M. *et al.* High-Throughput Mapping of Single-Neuron Projections by Sequencing of Barcoded RNA. *Neuron* **91**, 975–987 (2016).

33. Chung, K. *et al.* Structural and molecular interrogation of intact biological systems. *Nature* **497**, 332–337 (2013).

34. Renier, N. *et al.* Mapping of Brain Activity by Automated Volume Analysis of Immediate Early Genes. *Cell* **165**, 1789–1802 (2016).

35. Berg, S. *et al.* ilastik: interactive machine learning for (bio)image analysis. *Nat. Methods* **16**, 1226–1232 (2019).

36. Friedmann, D. *et al.* Mapping mesoscale axonal projections in the mouse brain using a 3D convolutional network. *Proc. Natl. Acad. Sci.* (2020) doi:10.1073/pnas.1918465117.

37. Tervo, D. G. R. *et al.* A Designer AAV Variant Permits Efficient Retrograde Access to Projection Neurons. *Neuron* (2016) doi:10.1016/j.neuron.2016.09.021.

38. Anastasiades, P. G. & Carter, A. G. Circuit organization of the rodent medial prefrontal cortex. *Trends Neurosci.* **44**, 550–563 (2021).

39. Chi, J., Crane, A., Wu, Z. & Cohen, P. Adipo-Clear: A Tissue Clearing Method for Three-Dimensional Imaging of Adipose Tissue. *J. Vis. Exp.* (2018) doi:10.3791/58271.

40. Chi, J. *et al.* Three-Dimensional Adipose Tissue Imaging Reveals Regional Variation in Beige Fat Biogenesis and PRDM16-Dependent Sympathetic Neurite Density. *Cell Metab.* **27**, 226-236.e3 (2018).

41. Kramer, D. J. *et al.* Generation of a DAT-P2A-Flpo mouse line for intersectional genetic targeting of dopamine neuron subpopulations. *Cell Rep.* **35**, 109123 (2021).

42. Kebschull, J. M. *et al.* Cerebellar nuclei evolved by repeatedly duplicating a conserved cell-type set. *Science.* **370**, (2020).

43. DeNardo, L. A. *et al.* Temporal evolution of cortical ensembles promoting remote memory retrieval. *Nat. Neurosci.* **22**, 460–469 (2019).

44. Anastasiades, P. G., Boada, C. & Carter, A. G. Cell-Type-Specific D1 Dopamine Receptor Modulation of Projection Neurons and Interneurons in the Prefrontal Cortex. *Cereb. Cortex* **29**, 3224–3242 (2019).

45. Oh, S. W. *et al.* A mesoscale connectome of the mouse brain. *Nature* **508**, 207–214 (2014).

46. Ährlund-Richter, S. *et al.* A whole-brain atlas of monosynaptic input targeting four different cell types in the medial prefrontal cortex of the mouse. *Nat. Neurosci.* **22**, 657–668 (2019).

47. Wang, L. *et al.* Cell-Type-Specific Whole-Brain Direct Inputs to the Anterior and Posterior Piriform Cortex . *Frontiers in Neural Circuits* vol. 14 (2020).

48. Poo, C., Agarwal, G., Bonacchi, N. & Mainen, Z. F. Spatial maps in piriform cortex during olfactory navigation. *Nature* **601**, 595–599 (2022).

49. Harris, K. D. & Shepherd, G. M. G. The neocortical circuit: Themes and variations. *Nat. Neurosci.* **18**, 170–181 (2015).

50. Shepherd, G. M. G. Corticostriatal connectivity and its role in disease. *Nat. Rev. Neurosci.* **14**, 278–291 (2013).

51. Shepherd, G. M. G. & Svoboda, K. Laminar and columnar organization of ascending excitatory projections to layer 2/3 pyramidal neurons in rat barrel cortex. *J. Neurosci.* **25**, 5670–9 (2005).

52. Winnubst, J. *et al.* Reconstruction of 1,000 Projection Neurons Reveals New Cell Types and Organization of Long-Range Connectivity in the Mouse Brain. *Cell* **179**, 268-281.e13 (2019).

53. Collins, D. P., Anastasiades, P. G., Marlin, J. J. & Carter, A. G. Reciprocal Circuits Linking the Prefrontal Cortex with Dorsal and Ventral Thalamic Nuclei. *Neuron* **98**, 366-379.e4 (2018).

54. Anastasiades, P. G., Marlin, J. J. & Carter, A. G. Cell-Type Specificity of Callosally Evoked Excitation and Feedforward Inhibition in the Prefrontal Cortex. *Cell Rep.* **22**, 679–692 (2018).

55. Nakayama, H., Ibañez-Tallon, I. & Heintz, N. Cell-Type-Specific Contributions of Medial Prefrontal Neurons to Flexible Behaviors. *J. Neurosci.* **38**, 4490–4504 (2018).

56. Gerfen, C. R., Paletzki, R. & Heintz, N. GENSAT BAC cre-recombinase driver lines to study the functional organization of cerebral cortical and basal ganglia circuits. *Neuron* **80**, 1368–1383 (2013).

57. Park, J. & Moghaddam, B. Risk of punishment influences discrete and coordinated encoding of reward-guided actions by prefrontal cortex and VTA neurons. *Elife* **6**, (2017).

58. Lucantonio, F. *et al.* Aversive stimuli bias corticothalamic responses to motivationally significant cues. *Elife* **10**, (2021).

59. Mitchell, A. S. The mediodorsal thalamus as a higher order thalamic relay nucleus important for learning and decision-making. *Neurosci. Biobehav. Rev.* **54**, 76–88 (2015).

60. Huang, W. C., Zucca, A., Levy, J. & Page, D. T. Social Behavior Is Modulated by Valence-Encoding mPFC-Amygdala Sub-circuitry. *Cell Rep.* **32**, 107899 (2020).

61. Guadagno, A., Belliveau, C., Mechawar, N. & Walker, C.-D. Effects of Early Life Stress on the Developing Basolateral Amygdala-Prefrontal Cortex Circuit: The Emerging Role of Local Inhibition and Perineuronal Nets . *Frontiers in Human Neuroscience* vol. 15 (2021).

62. Dong, M. *et al.* A failed top-down control from the prefrontal cortex to the amygdala in generalized anxiety disorder: Evidence from resting-state fMRI with Granger causality analysis. *Neurosci. Lett.* **707**, 134314 (2019).

63. Clauss, J. A., Benningfield, M. M., Rao, U. & Blackford, J. U. Altered Prefrontal Cortex Function Marks Heightened Anxiety Risk in Children. *J. Am. Acad. Child Adolesc. Psychiatry* **55**, 809–816 (2016).

64. Johnstone, T., van Reekum, C. M., Urry, H. L., Kalin, N. H. & Davidson, R. J. Failure to Regulate: Counterproductive Recruitment of Top-Down Prefrontal-Subcortical Circuitry in Major Depression. *J. Neurosci.* **27**, 8877 LP – 8884 (2007).

65. Courchesne, E. & Pierce, K. Why the frontal cortex in autism might be talking only to itself: local over-connectivity but long-distance disconnection. *Curr. Opin. Neurobiol.* **15**, 225–230 (2005).

66. Li, Q. *et al.* Decreased interhemispheric functional connectivity rather than corpus callosum volume as a potential biomarker for autism spectrum disorder. *Cortex* **119**, 258–266 (2019).

67. Yao, S., Becker, B. & Kendrick, K. M. Reduced Inter-hemispheric Resting State Functional Connectivity and Its Association With Social Deficits in Autism . *Frontiers in Psychiatry* vol. 12 (2021).

68. Weston, C. S. E. Four Social Brain Regions, Their Dysfunctions, and Sequelae, Extensively Explain Autism Spectrum Disorder Symptomatology. *Brain Sciences* vol. 9 (2019).

69. Collins, D. P., Anastasiades, P. G., Marlin, J. J. & Carter, A. G. Reciprocal Circuits Linking the Prefrontal Cortex with Dorsal and Ventral Thalamic Nuclei. *Neuron* **98**, 366-379.e4 (2018).

70. McGarry, L. M. & Carter, A. G. Prefrontal Cortex Drives Distinct Projection Neurons in the Basolateral Amygdala. *Cell Rep.* **21**, 1426–1433 (2017).

71. Gehrlach, D. A. *et al.* A whole-brain connectivity map of mouse insular cortex. *Elife* **9**, e55585 (2020).

72. Beier, K. T. *et al.* Circuit Architecture of VTA Dopamine Neurons Revealed by Systematic Input-Output Mapping. *Cell* **162**, 622–634 (2015).

73. Ährlund-Richter, S. *et al.* A whole-brain atlas of monosynaptic input targeting four different cell types in the medial prefrontal cortex of the mouse. *Nat. Neurosci.* (2019) doi:10.1038/s41593-019-0354-y.

74. Schwarz, L. A. *et al.* Viral-genetic tracing of the input-output organization of a central noradrenaline circuit. *Nature* **524**, 88–92 (2015).

75. Klein, S., Staring, M., Murphy, K., Viergever, M. A. & Pluim, J. P. W. Elastix: A toolbox for intensity-based medical image registration. *IEEE Trans. Med. Imaging* (2010) doi:10.1109/TMI.2009.2035616.

76. Wang, Q. *et al.* The Allen Mouse Brain Common Coordinate Framework: A 3D Reference Atlas. *Cell* **181**, 936-953.e20 (2020).

77. Perens, J. *et al.* An Optimized Mouse Brain Atlas for Automated Mapping and Quantification of Neuronal Activity Using iDISCO+ and Light Sheet Fluorescence Microscopy. *Neuroinformatics* **19**, 433–446 (2021).

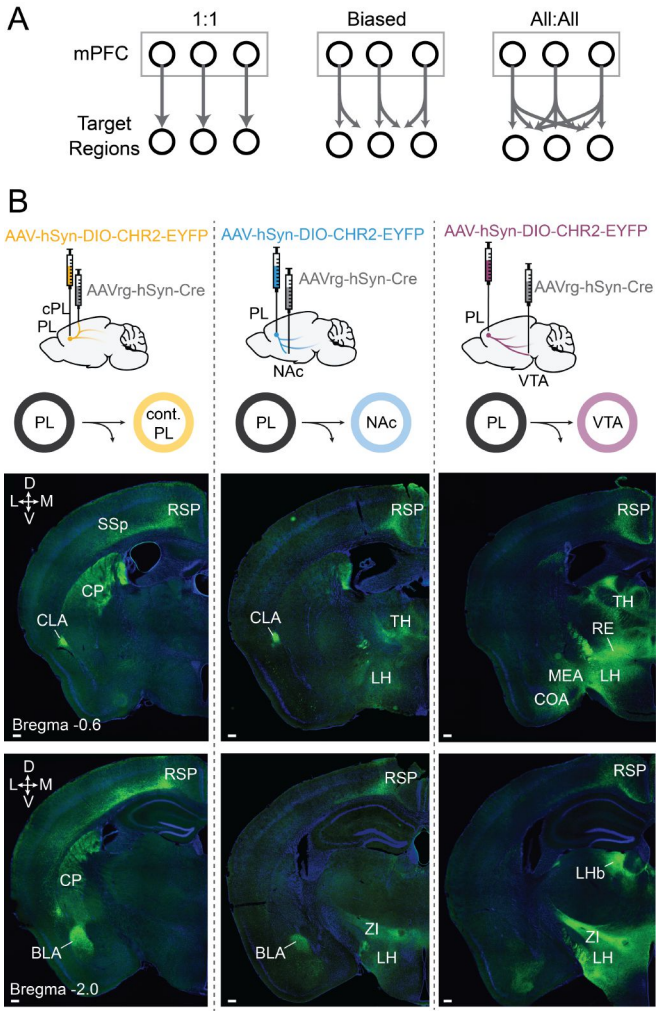


**Figure 1. Viral strategy for whole-brain collateralization mapping.**
(A) Potential mPFC efferent connectivity patterns.
(B) Schematic of stereotaxic injection strategy for labeling PL-cPL, PL-NAc, and PL-VTA neurons (top) and coronal brain sections showing distinct axonal collateralization patterns for each cell type (bottom). Scale bars, 200um. Abbreviations: CLA, claustrum; CP, caudate putamen; SSp, primary somatosensory cortex; TH, thalamus; LH, lateral hypothalamus; RE, nucleus reuniens; RSP, retrosplenial cortex, MEA, medial amygdala; COA, cortical amygdala; BLA, basolateral amygdala; ZI, zona incerta; LHb, lateral habenula.

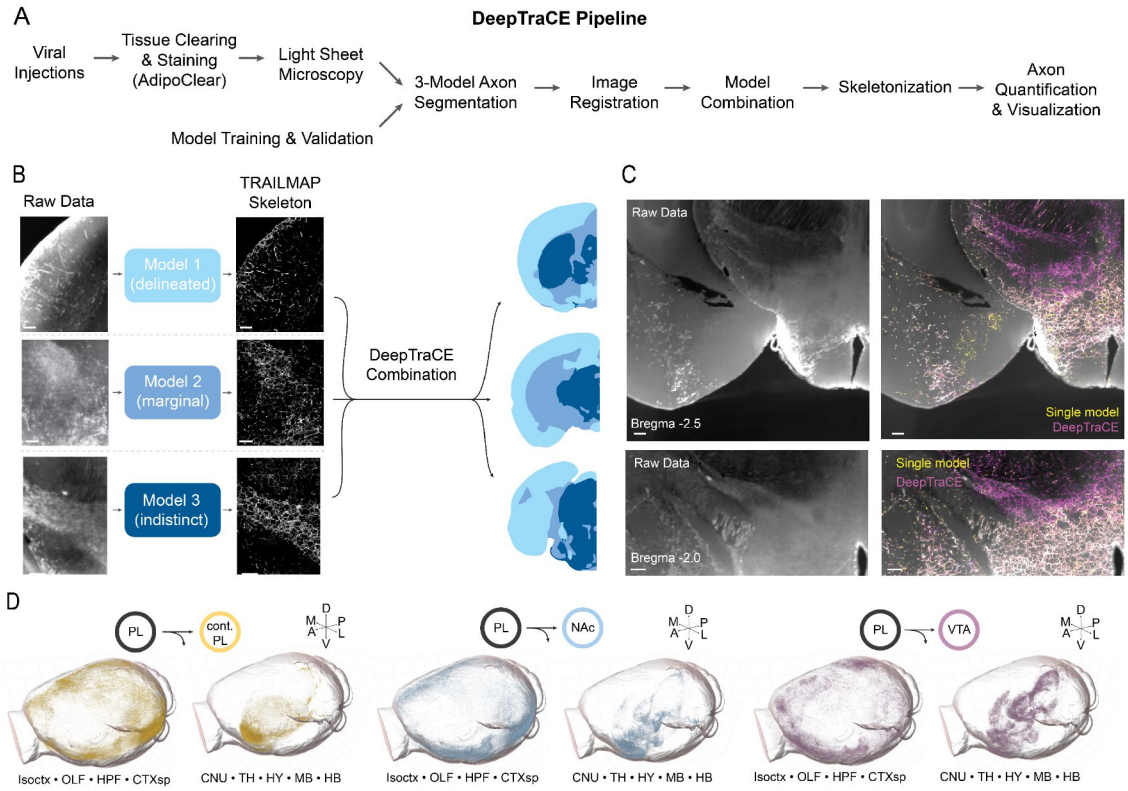


**Figure 2. DeepTraCE workflow**

(A) Overview of DeepTraCE workflow

(B) Demonstration of segmentation using 3 different models followed by concatenation

(C) Overlay of raw data and axon segmentation using single model or DeepTraCE concatenated models

(D) DeepTraCE segmentation of superficial (left) and deep (right) brain structures for each cell type. Scale bars, 200um. Abbreviations: Isoctx, isocortex; OLF, olfactory areas; HPF, hippocampal formation; CTXsp, cortical subplate; CNU, cerebral nuclei; HY, hypothalamus; MB, midbrain; HB, hindbrain

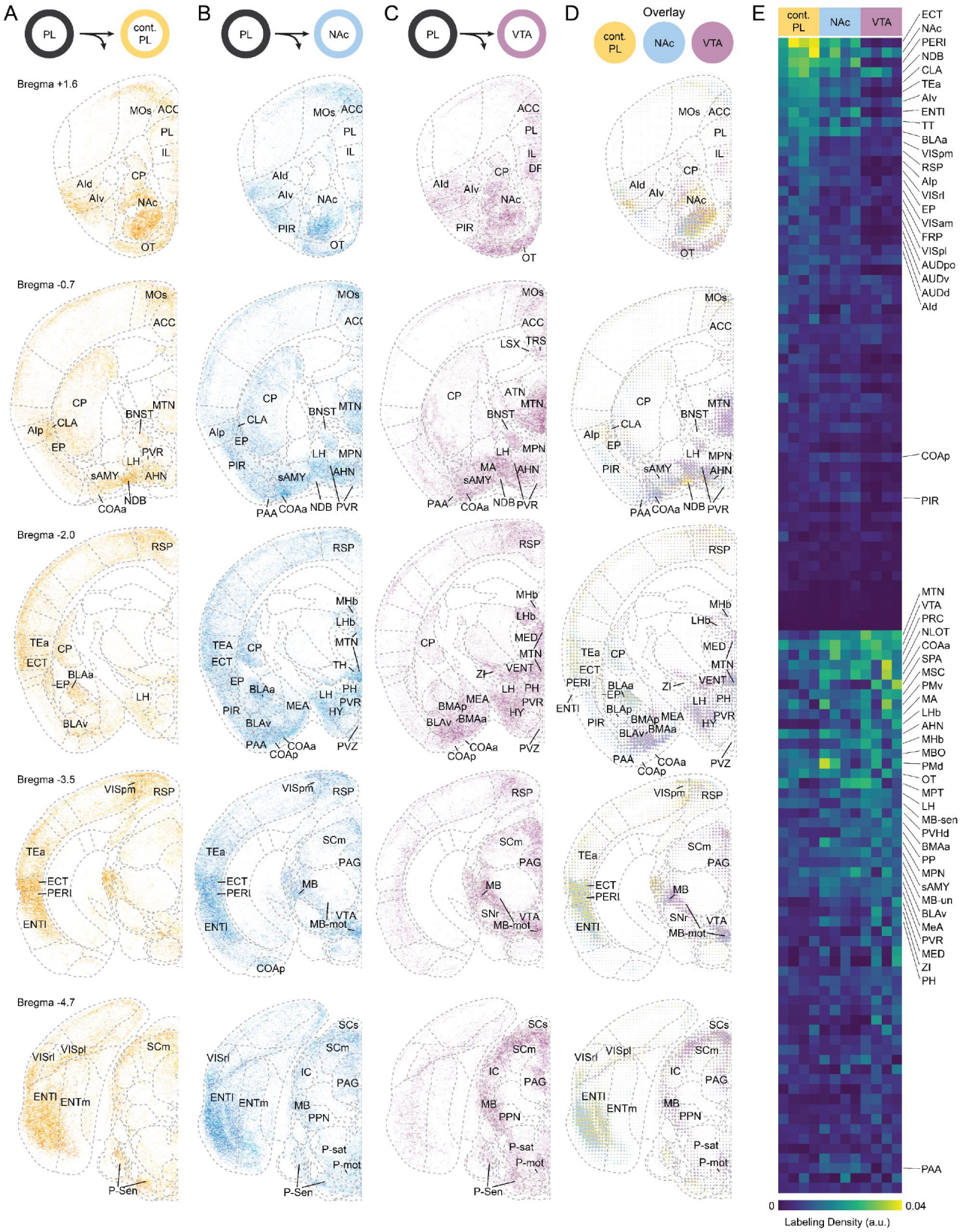
A
PL
cont. PL
B
PL
NAc
C
PL
VTA
D
Overlay
cont. PL
NAc
VTA
E
cont. PL
NAc
VTA
Bregma +1.6
Bregma -0.7
Bregma -2.0
Bregma -3.5
Bregma -4.7
ECT
NAc
PERI
NDB
CLA
TEa
Alv
ENTI
TT
BLAa
VISpm
RSP
Alp
VISrl
EP
VISam
FRP
VISpl
AUDpo
AUDv
AUDd
Ald
COAp
PIR
MTN
VTA
PRC
NLOT
COAa
SPA
MSC
PMv
MA
LHb
AHN
MHb
MBO
PMd
OT
MPT
LH
MB-sen
PVHd
BMAa
PP
MPN
sAMY
MB-un
BLAv
MeA
PVR
MED
ZI
PH
PAA
0
0.04
Labeling Density (a.u.)

**Figure 3. Visualization and quantification of brain-wide projection patterns of PL-cPL, PL-NAc and PL-VTA neurons.**
(A–C) Single 10um coronal optical sections of thinned axons registered to the standardized brain atlas. Each image represents 4 overlaid brains from each type.
(D) Dotogram overlay of 3 cell types. Innvervation by cPL-, NAc- and VTA-projecting PL neurons shown in yellow, blue and purple, respectively.
(E) Heatmap of relative labeling density (normalized to region volume and gross label content per brain) across 140 regions defined by the Allen Brain Atlas.
See supplemental figures 3-6 for related data.

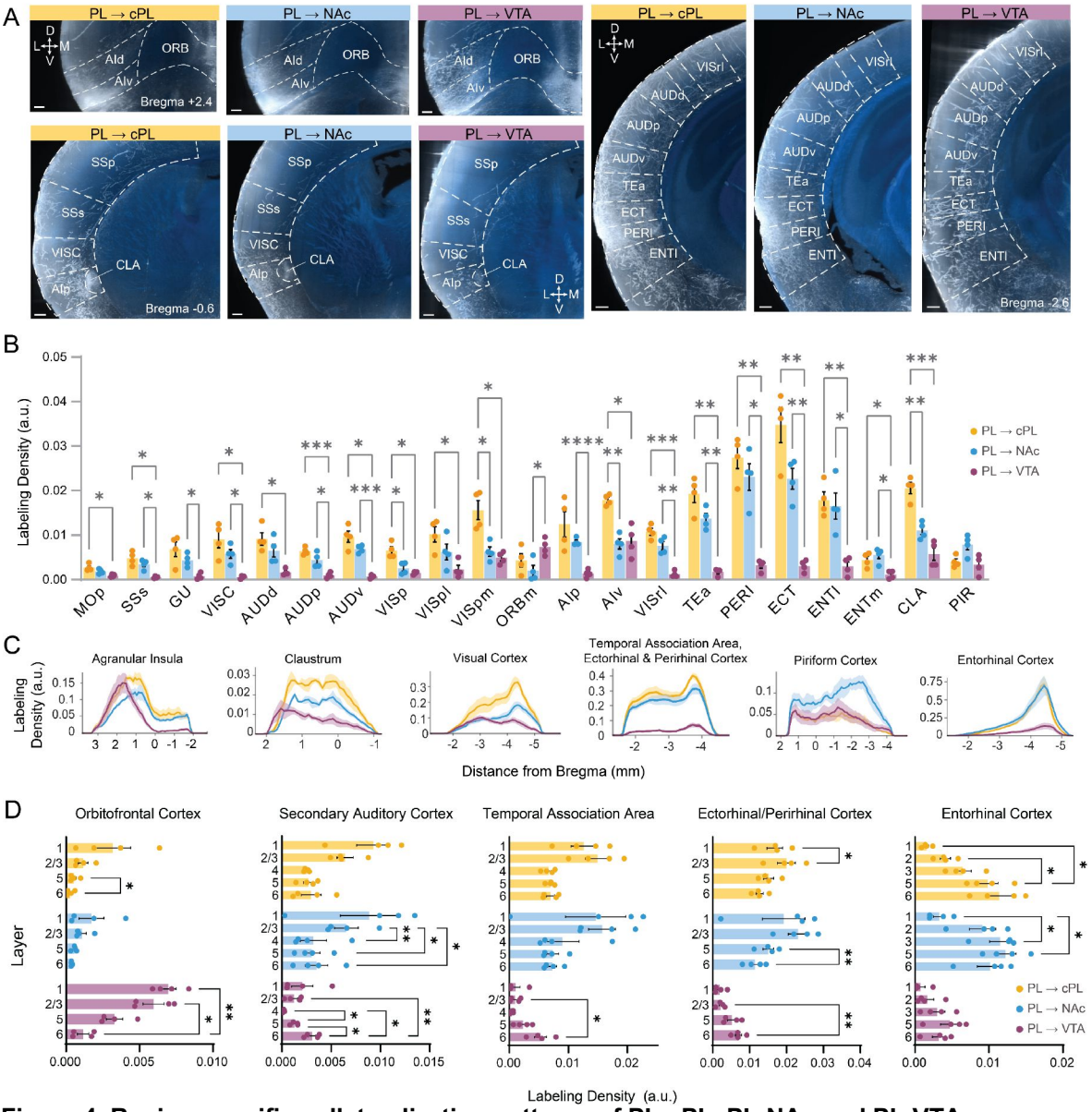


**Figure 4. Region-specific collateralization patterns of PL-cPL, PL-NAc and PL-VTA neurons**
(A) Coronal view of 100um z-projections of raw 640nm (axons, white) and 488nm (autofluorescence, blue) channels from individual brains. Images show cell-type specific innervation patterns in anterior (left) and posterior (right) cortical areas.
(B) Quantification of labeled axons in 21 cortex and subplate regions (n=4/group).
(C) Visualizations of axonal innervation density along the anterior-posterior axis in select regions. PL-cPL, PL-NAc and PL-VTA neurons coded in yellow, blue and purple, respectively.
(D) Layer distributions of axonal innervation in select cortical target regions.
See Table 1,2 for abbreviations and detailed statistics. 2-way ANOVA with Tukey's post-hoc multiple comparison test. Descriptive statistics: mean ± S.E.M. *$P$<0.05, **$P$<0.01, ***$P$<0.001.

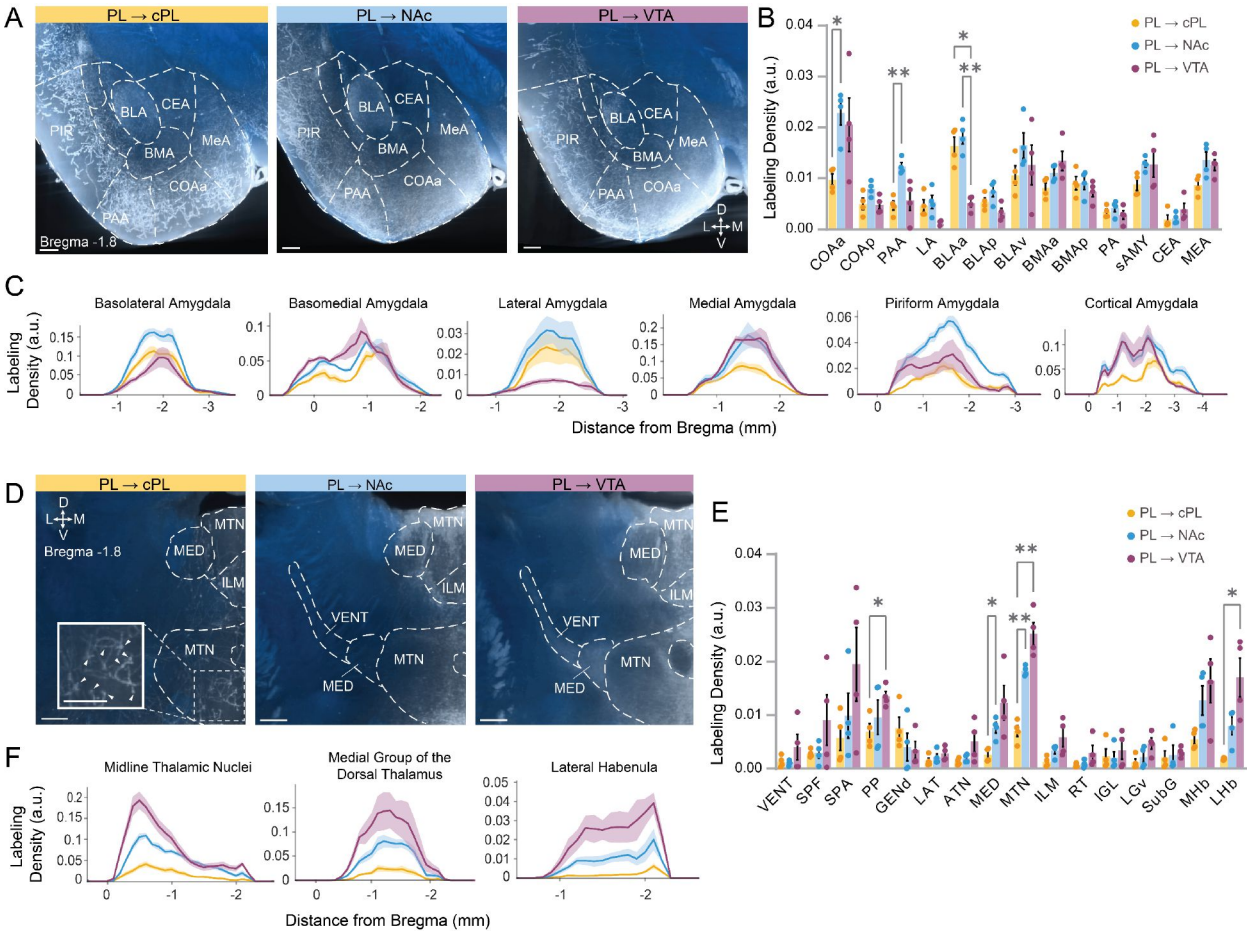


**Figure 5. Collateralization patterns of PL-cPL, PL-NAc and PL-VTA neurons in amygdala and thalamus**

(A) Raw images showing axons in the amygdalar complex.
(B) Quantification of labeled axon density in amygdala subregions (n=4/group).
(C) Quantification of axonal innervation density along the anterior-posterior axis of a given region. PL-cPL, PL-NAc and PL-VTA neurons coded in yellow, blue and purple, respectively.
(D) Raw images showing axons in thalamic nuclei.
(E) Quantification of labeled axons in thalamic nuclei (n=4/group).
(F) Quantification of axonal innervation density along the anterior- posterior axis of a given region. Arrows indicate varicosities reminiscent of synaptic release sites. PL-cPL, PL-NAc and PL-VTA neurons coded in yellow, blue and purple, respectively.
See Tables 1, 2 for abbreviations and detailed statistics. 2-way ANOVA with Tukey's post-hoc multiple comparison test. Descriptive statistics: mean ± S.E.M. *$P$<0.05, **$P$<0.01, ***$P$<0.001.

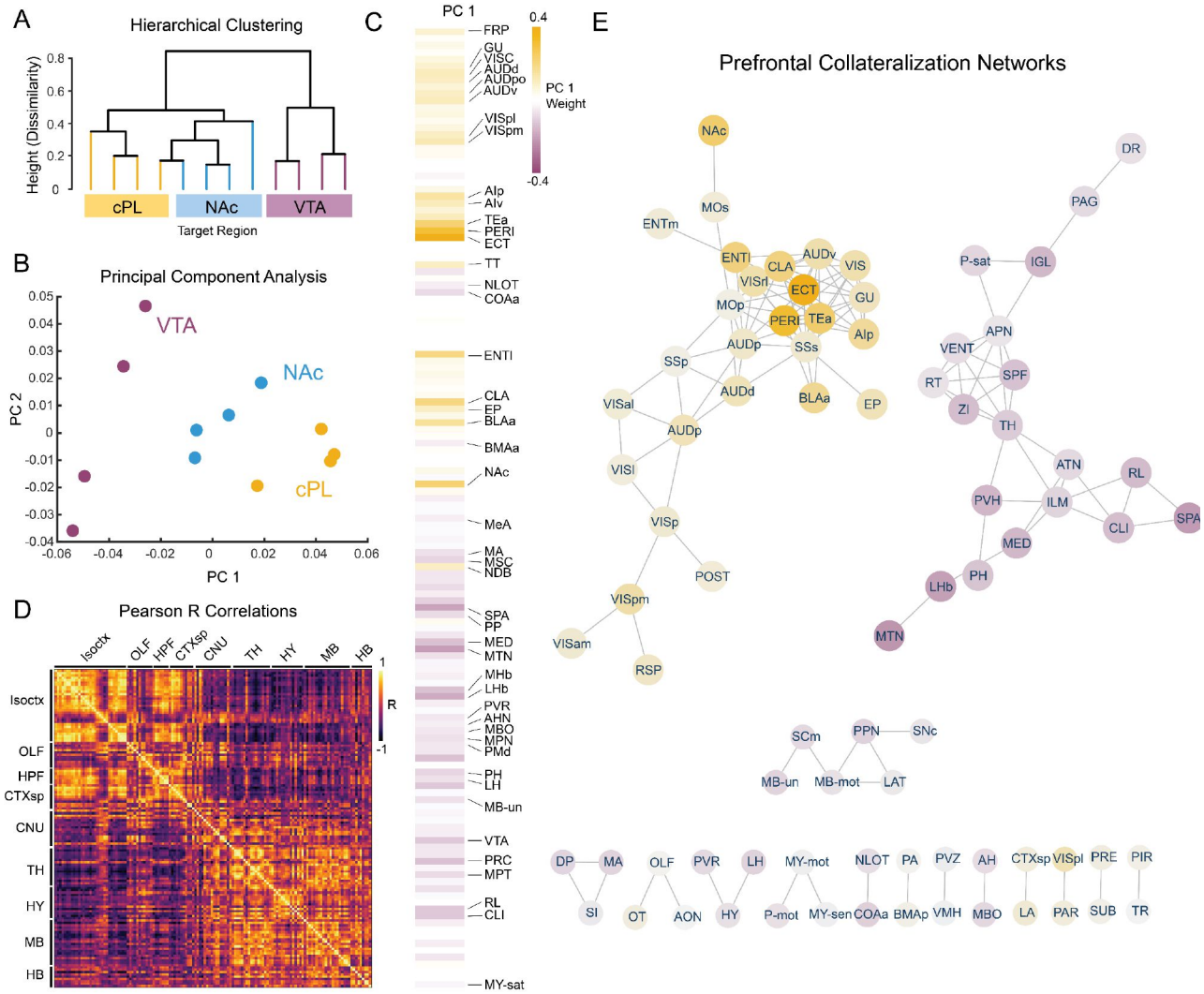


**Figure 6. Hierarchical clustering and PCA analysis reveals cell-type specific output organization**
(A) Dendrogram of hierarchical clustering of regional axon quantifications from 12 mice, colored by target region.
(B) Locations of individual mice projected in principal component (PC) space defined by the first two PCs (arbitrary PC units, cPL, *n*=4; NAc, *n*=4; VTA, *n*=4).
(C) Loadings for PC1 (arbitrary PC weight units)
(D) Heatmap of Pearson's R correlations between regional axon quantifications. PL-cPL, PL-NAc and PL-VTA neurons were all included in correlation calculation. Each square in the heatmap corresponds to the strength of correlation between two brain regions, with brighter values indicating stronger correlation. See Tables 1 for abbreviations.
(E) Network visualization of correlations from (D) with $P<0.05$ and $R>0.85$, colored by PC1 weights from (C). Default Cytoscape layout was used for visualization.

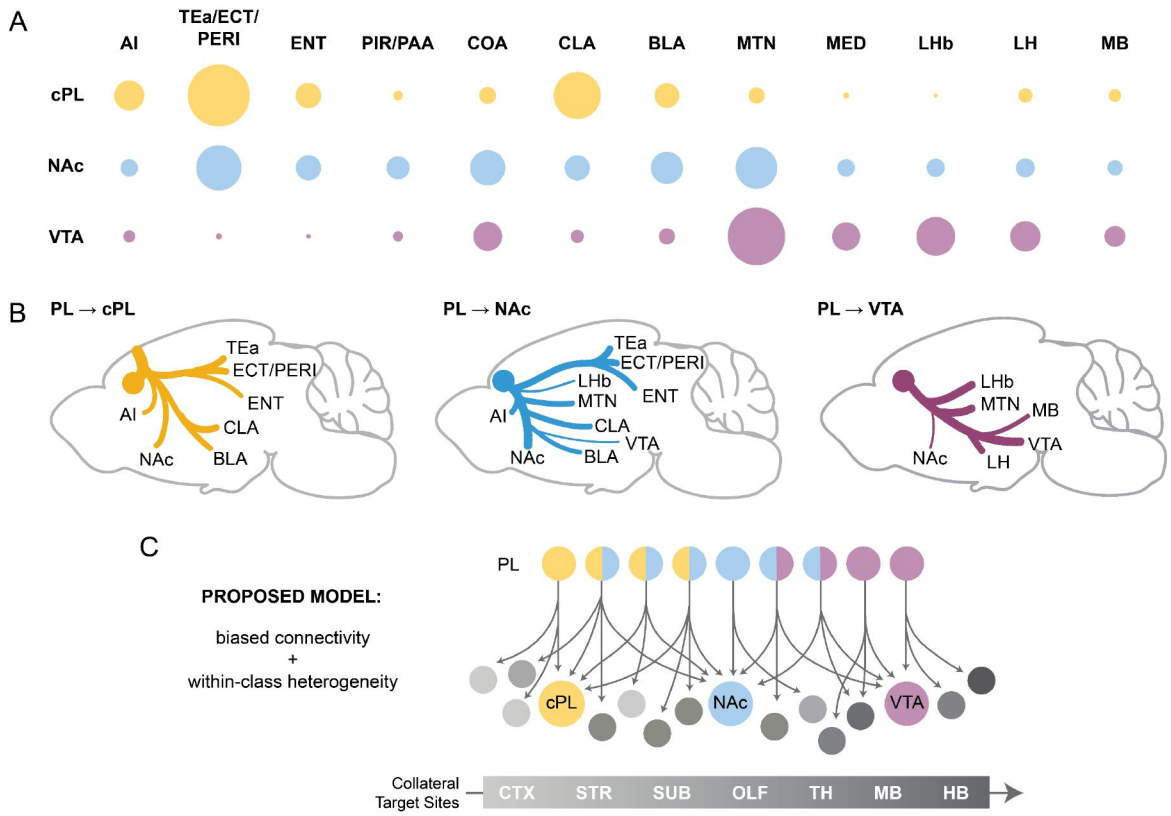


**Figure 7. Summary of Findings**

(A) Visualization of collateralization density in key targets of PL–cPL, PL–NAc, and PL–VTA neurons. Dot radius correlates with average normalized labeling density within a region.
(B) Schematic of whole-brain collateralization patterns of PL–cPL, PL–NAc, and PL–VTA neurons.
(C) Proposed model of prefrontal efferent connectivity patterns.
See Table 1 for abbreviations.

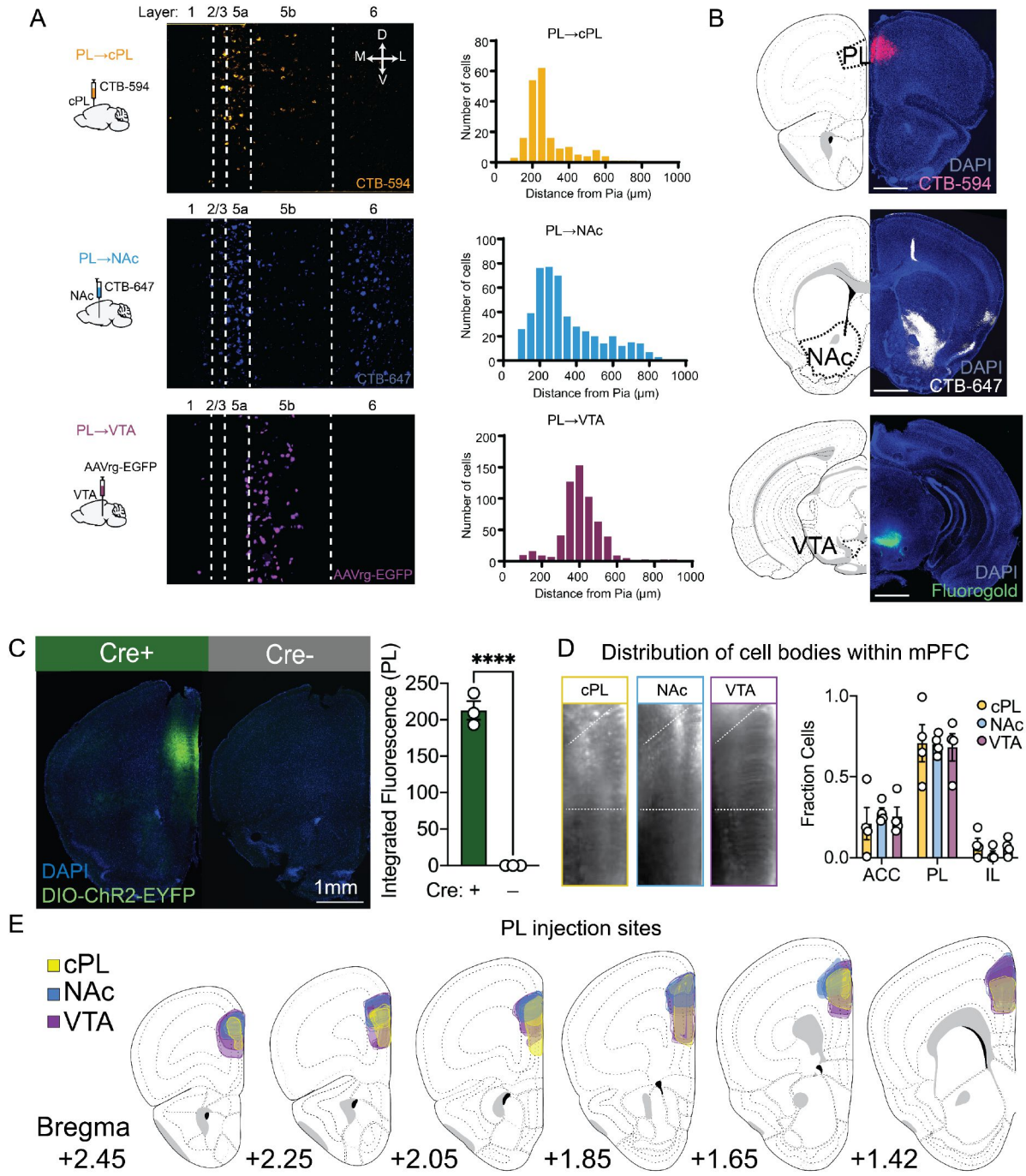


**Supplemental Figure 1. Validation of Cre-Dependent Virus and Injection Site Mapping. Related to Figure 1.**

(A) Layer distributions of prelimbic neurons retrogradely labeled via injections of CTB-594, CTB-647, and AAVrg-EGFP in cPL, NAc, and VTA, respectively.

(B) Representative images of target sites (cPL, NAc and VTA) visualized with Cholera Toxin Subunit B and Fluorogold.

(C) Representative Coronal Sections sections of brains injected with AAVrg-Cre and AAV-DIO-ChR2-EYPF (left) or AAV-DIO-ChR2-EFYP in the absence of Cre and quantification of fluorescence in PL.

(D) Raw fluorescence images from LSFM showing mPFC and quantifications of cell body numbers within ACC, PL and IL.

(E) Maps of starter cells in mPFC for each cell type

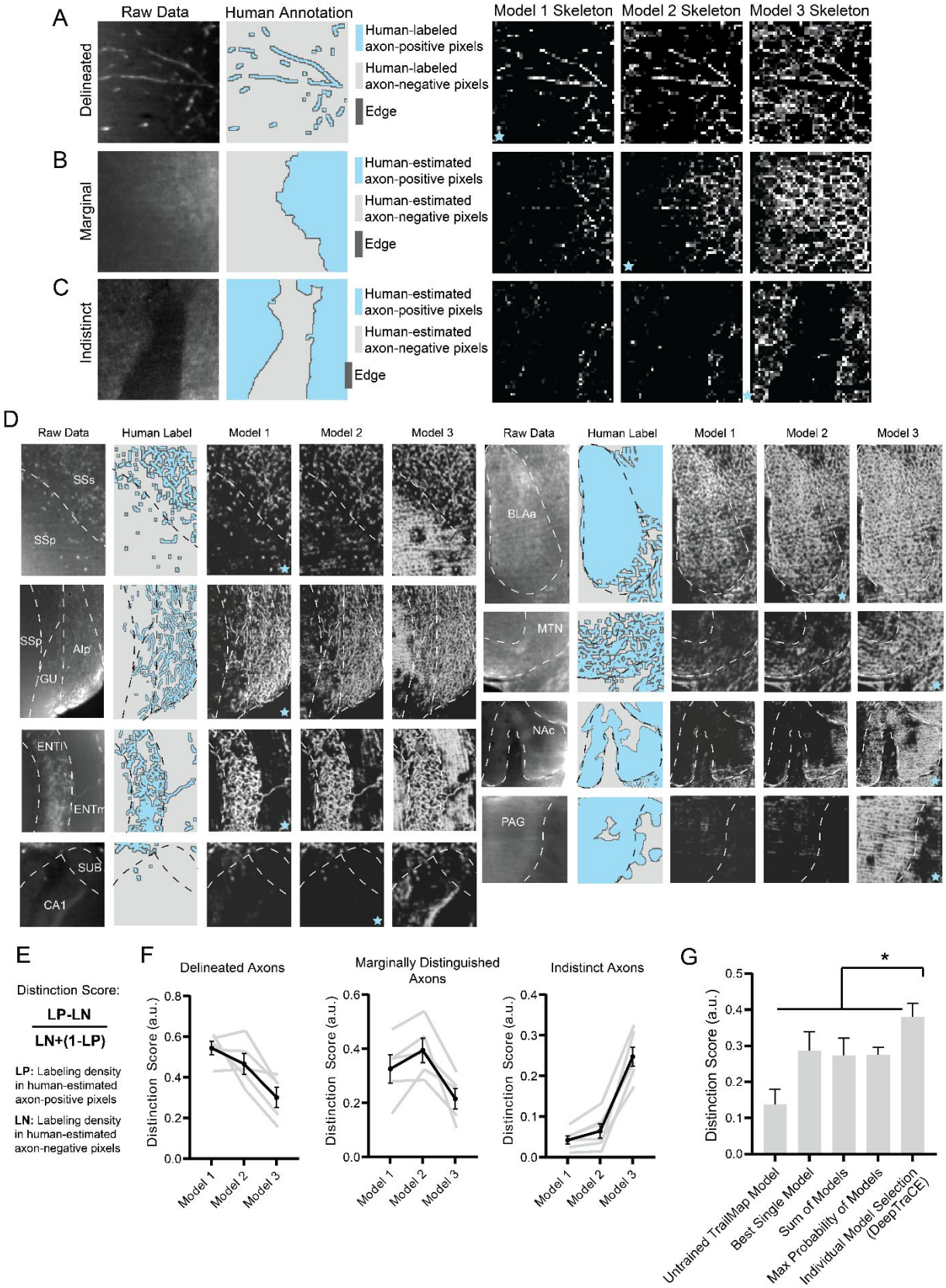
A
Raw Data
Human Annotation
Model 1 Skeleton
Model 2 Skeleton
Model 3 Skeleton
Delineated
Human-labeled axon-positive pixels
Human-labeled axon-negative pixels
Edge
B
Marginal
Human-estimated axon-positive pixels
Human-estimated axon-negative pixels
Edge
C
Indistinct
Human-estimated axon-positive pixels
Human-estimated axon-negative pixels
Edge
D
Raw Data
Human Label
Model 1
Model 2
Model 3
SSs
SSp
BLAa
SSp
AIp
GU
MTN
ENTl
ENTm
NAc
PAG
SUB
CA1
E
Distinction Score:
LP-LN
LN+(1-LP)
LP: Labeling density in human-estimated axon-positive pixels
LN: Labeling density in human-estimated axon-negative pixels
F
Delineated Axons
Marginally Distinguished Axons
Indistinct Axons
Distinction Score (a.u.)
Model 1
Model 2
Model 3
G
*
Distinction Score (a.u.)
Untrained TrailMap Model
Best Single Model
Sum of Models
Max Probability of Models
Individual Model Selection (DeepTraCE)

**Supplemental Figure S2. Validation of DeepTraCE Pipeline. Related to Figure 2.**

(A-C) Single 500x500um planes of raw axon data, human annotation, and skeletons from Models 1, 2, and 3 in images of delineated, marginally delineated, and indistinct axons. Blue stars indicate model fine-tuned for segmentation at corresponding tissue depth.
(D) Representative images of raw data, human annotation, and probability maps from each model for regions assigned to Models 1, 2, and 3. Blue stars indicate model selected for segmentation of this region in DeepTraCE.
(E) Equation for distinction score. Higher score indicates higher distinction between axon-positive and axon-negative region and lower rate of false positives and false negatives.
(F) Distinction score produced by models 1, 2, and 3 for images of delineated, marginally delineated, and indistinct axons. Repeated-measures one-way ANOVA (Delineated: $F=8.503$, $p=0.0257$; Marginal: $F=7.753$, $p=0.0309$; Indistinct: $F=73.76$, $p=0.0001$).
(G) Comparison of DeepTraCE with alternate segmentation and model combination strategies. Repeated measures one-way ANOVA with Dunnett's multiple comparisons test ($F=14.46$, $p<0.0001$). See Table 3 for detailed statistics.
Descriptive statistics: mean ± SEM. *$P<0.05$.

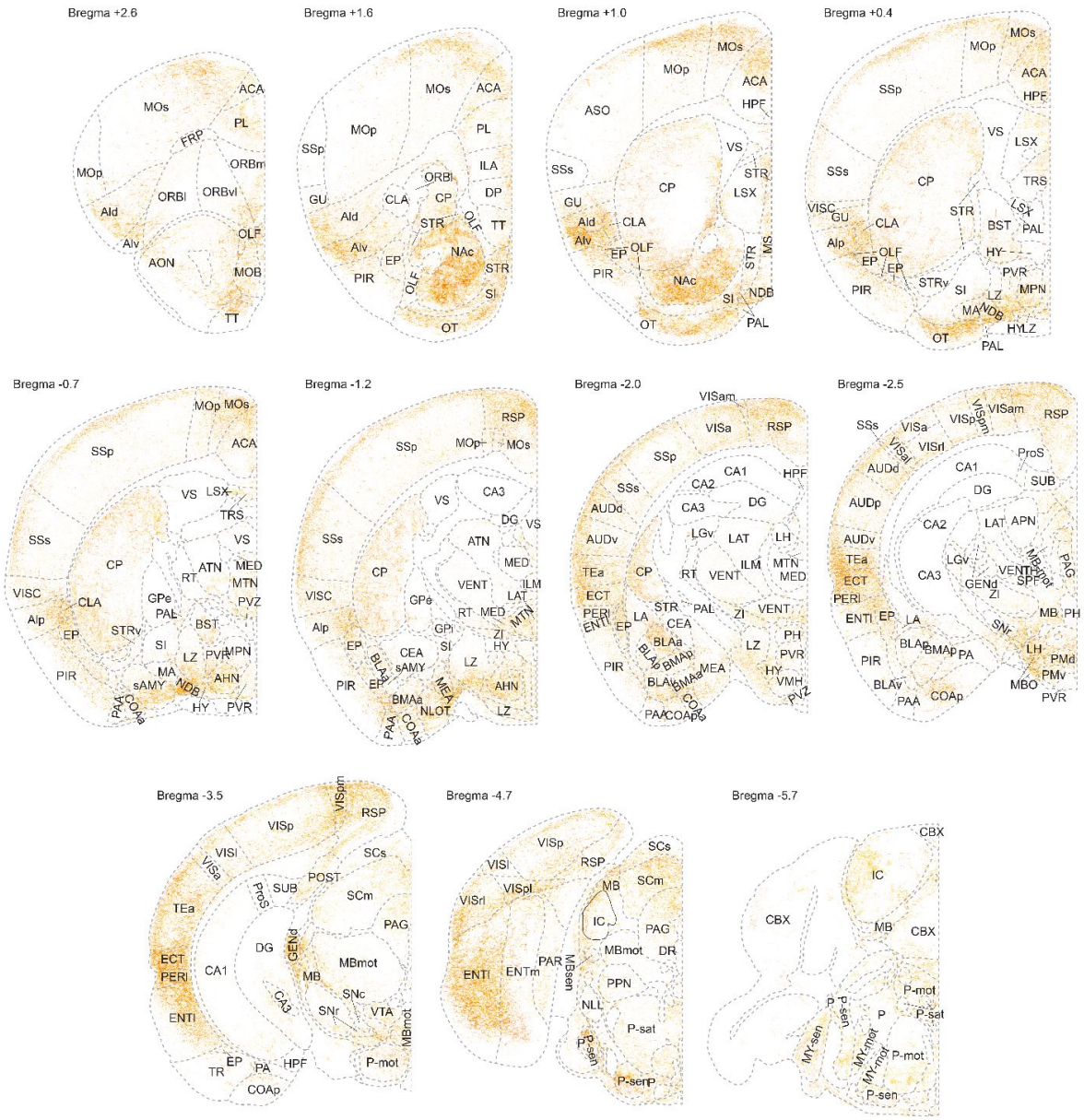


**Supplemental Figure S3. Whole-brain PL–cPL collateralization patterns. Related to Figure 3.**

Eleven fully annotated 10um coronal optical sections of skeletonized images registered to the standardized brain atlas. Each image represents 4 overlaid PL–cPL brains. Sections from Bregma values +1.6, +0.7, -2.0, -3.5, and -4.7 are the same as shown in Figure 3.

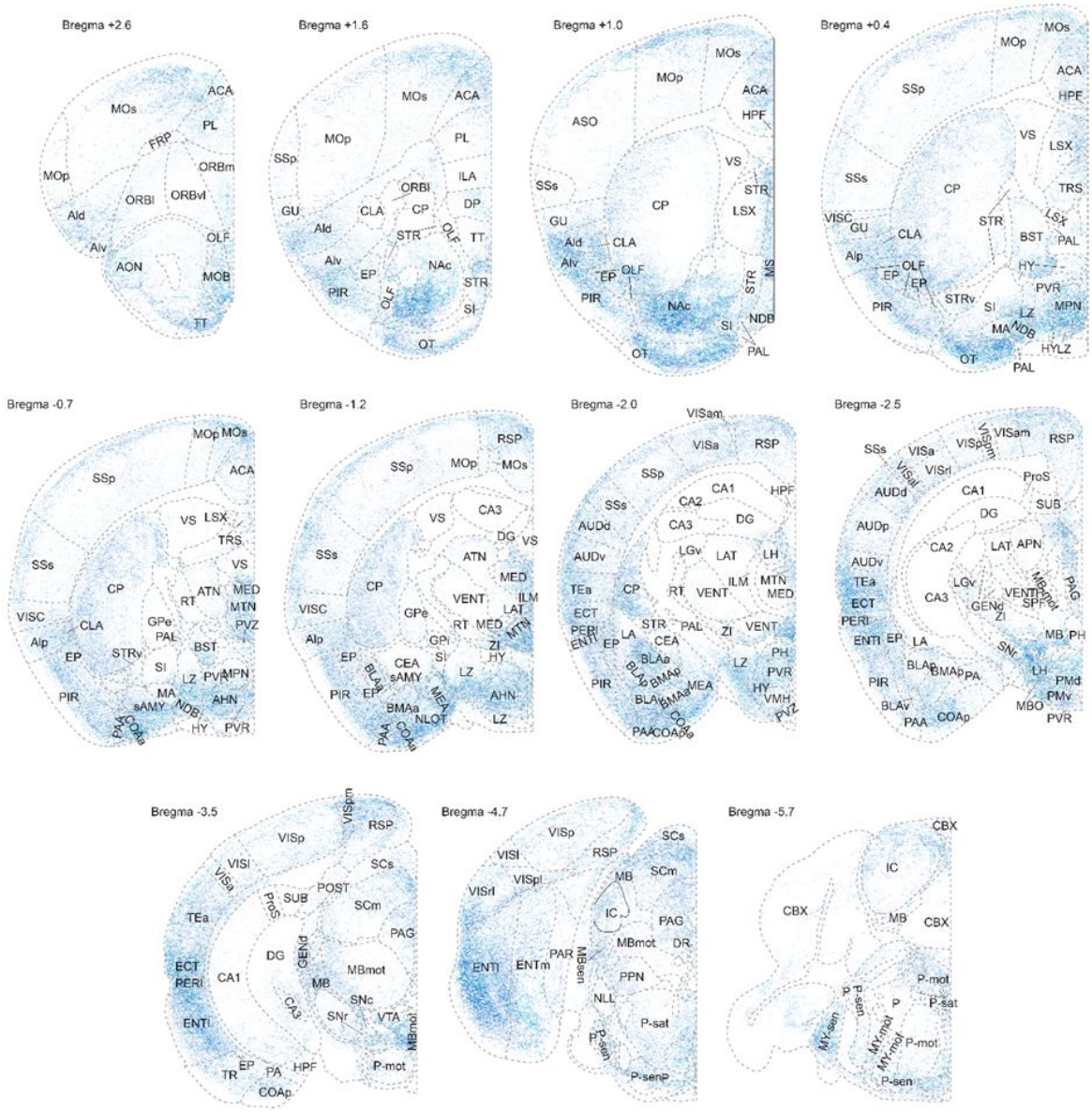


**Supplemental Figure S4. Whole-brain PL–NAc collateralization patterns. Related to Figure 3.**

Eleven fully annotated 10um coronal optical sections of skeletonized images registered to the standardized brain atlas. Each image represents 4 overlaid PL–NAc brains. Sections from Bregma values +1.6, +0.7, -2.0, -3.5, and -4.7 are the same as shown in Figure 3.

**Supplemental Figure S5. Whole-brain PL–VTA collateralization patterns. Related to Figure 3.**

Eleven fully annotated 10um coronal optical sections of skeletonized images registered to the standardized brain atlas. Each image represents 4 overlaid PL–VTA brains. Sections from Bregma values +1.6, +0.7, -2.0, -3.5, and -4.7 are the same as shown in Figure 2.

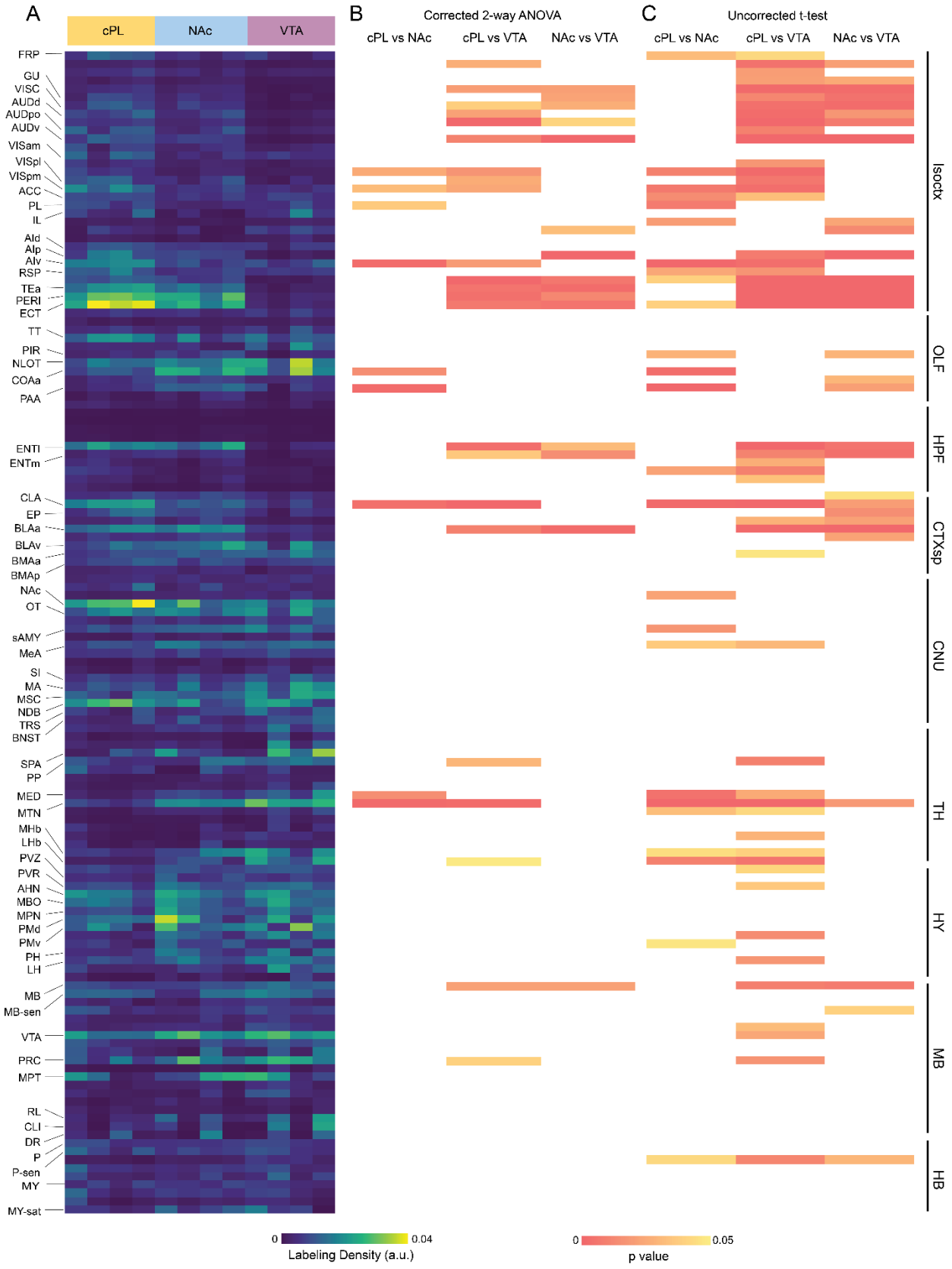
A
cPL
NAc
VTA
FRP
GU
VISC
AUDd
AUDpo
AUDv
VISam
VISpl
VISpm
ACC
PL
IL
AId
AIp
AIv
RSP
TEa
PERI
ECT
TT
PIR
NLOT
COAa
PAA
ENTl
ENTm
CLA
EP
BLAa
BLAv
BMAa
BMAp
NAc
OT
sAMY
MeA
SI
MA
MSC
NDB
TRS
BNST
SPA
PP
MED
MTN
MHb
LHb
PVZ
PVR
AHN
MBO
MPN
PMd
PMv
PH
LH
MB
MB-sen
VTA
PRC
MPT
RL
CLI
DR
P
P-sen
MY
MY-sat
B
Corrected 2-way ANOVA
cPL vs NAc
cPL vs VTA
NAc vs VTA
C
Uncorrected t-test
cPL vs NAc
cPL vs VTA
NAc vs VTA
Isoctx
OLF
HPF
CTXsp
CNU
TH
HY
MB
HB
0
0.04
Labeling Density (a.u.)
0
0.05
p value

**Supplemental Figure S6. Whole-brain collateralization data and statistics ordered by Allen Brain Atlas ontology. Related to Figure 3. See also Table 2.**

(A) Heatmap from Figure 3 ordered by Allen Brain Atlas ontology.
(B) Heatmap of p values from 2-way ANOVA with Tukey's multiple comparison correction for all brain regions.
(C) Heatmap of uncorrected p values from unpaired t-tests between cPL and NAc, cPL and VTA, and NAc and VTA.

| | |
|---|---|
| ACC | Anterior Cingulate Cortex |
| AH | Anterior Hypothalamic Area |
| AHN | Anterior Hypothalamic Nucleus |
| AId | Agranular Insula, dorsal part |
| AIp | Agranular Insula, posterior part |
| AIv | Agranular Insula, ventral part |
| ATN | Anterior Group of the dorsal thalamus |
| AUDd | Dorsal auditory area |
| AUDp | Primary auditory area |
| AUDv | Ventral auditory area |
| BLA | Basolateral amygdala |
| BLAa | Basolateral amygdala, anterior part |
| BLAv | Basolateral amygdala, ventral part |
| BNST | Bed nucleus of the stria terminalis |
| CLA | Claustrum |
| cPL | Contralateral prelimbic area |
| CNU | Cerebral nuclei |
| COA | Cortical amygdalar area |
| COAa | Cortical amygdalar area, anterior part |
| COAp | Cortical amygdalar area, posterior part |
| CP | Caudate putamen |
| CTXsp | Cortical subplate |
| DP | Dorsal peduncular area |
| ECT | Ectorhinal cortex |
| ENTl | Entorhinal area, lateral part |
| ENTm | Entorhinal area, medial part |
| EP | Endopiriform nucleus |
| GENd | Geniculate group, dorsal thalamus |
| GU | Gustatory areas |
| HB | Hindbrain |
| HPF | Hippocampal formation |
| IC | Inferior colliculus |
| IGL | Intergeniculat leaflet of the lateral geniculate complex |
| IL | Infralimbic cortex |
| ILM | Intralaminar nucleus of the dorsal thalamus |
| Isoctx | Isocortex |
| LAT | Lateral geniculate nucleus |
| LGv | Ventral part of the lateral geniculate nucleus |
| LH | Lateral hypothalamus |
| LHb | Lateral habenula |
| MA | Magnocellular Nucleus |
| MB | Midbrain |
| MB-un | Midbrain-unlabeled |
| MBO | Mammillary body |
| MeA | Medial amygdala |
| MED | Medial group of the dorsal thalamus |
| MHb | Medial habenula |
| MOp | Primary motor area |
| MOs | Secondary motor area |
| mPFC | medial prefrontal cortex |
| MPN | Medial preoptic nucleus |
| MTN | Midline group of the dorsal thalamus |
| MY-mot | Medulla, motor related |
| MY-sen | Medulla, sensory related |
| NAc | Nucleus accumbens |
| NDB | Nucleus of the diagonal band |
| NLOT | Nucleus of the lateral olfactory tract |
| OLF | Olfactory tract |
| ORBm | Orbital area, medial part |
| OT | Olfactory tubercle |
| P-mot | Pons, motor related |
| P-Sat | Pons, behavioral state related |
| P-Sen | Pons, sensory related |
| PAA | Piriform-amygdalar area |
| PAG | Periaqueductal grey |
| PERI | Perirhinal area |
| PH | Posterior hypothalamic nucleus |
| PIR | Piriform area |
| PL | Prelimbic area |
| POST | Postrhinal area |
| PP | Peripeduncular nucleus |
| PPN | Pedunculopontine nucleus |
| PRC | Precommisural nucleus |
| PVHd | Paraventricular hypothalamic nucleus, descending division |
| PVR | Periventricular region |
| RE | Nucleus of reuniens |
| RSP | Retrosplenial cortex |
| RT | Reticular nucleus of the thalamus |
| sAMY | Striatum-like amygdala |
| SCm | Superior colliculus, motor related |
| SCs | Superior colliculus, senosry related |
| SNr | Substantia nigra, reticular part |
| SPA | Subparafascicular area |
| SPF | Subparafascicular nucleus |
| SSp | Primary somatosensory area |
| SSs | Secondary somatosensory area |
| SubG | Subgeniculate nucleus |
| TEa | Temporal association area |
| TH | Thalamus |
| TR | Postpiriform transition area |
| VENT | Ventral group of the dorsal thalamus |
| VISC | Visceral area |
| VISp | Primary visual area |
| VISpl | Posterolateral visual area |
| VISpm | Posteromedial visual area |
| VISrl | Rostrolateral visual area |
| VTA | Ventral tegmental area |
| ZI | Zona incerta |

**Table 1.** List of abbreviations

**Table 2.** Quantification of axon density by brain region**. Related to Figures 2,4,5.**

| Abbreviation | Allen Brain Atlas ID | Mean cPL | Mean NAc | Mean VTA | cPL Brain 1 | cPL Brain 2 | cPL Brain 3 | cPL Brain 4 | NAc Brain 1 | NAc Brain 2 | NAc Brain 3 | NAc Brain 4 | VTA Brain 1 | VTA Brain 2 | VTA Brain 3 | VTA Brain 4 | PC1 Weight | Corrected 2-way ANOVA: cPL vs NAc | Corrected 2-way ANOVA: cPL vs VTA | Corrected 2-way ANOVA: NAc vs VTA | Uncorrected p value: cPL vs NAc | Uncorrected p value: cPL vs VTA | Uncorrected p value: NAc vs VTA | Model Used |
|---|---|---|---|---|---|---|---|---|---|---|---|---|---|---|---|---|---|---|---|---|---|---|---|---|
| FRP | 'Frontal pole, cerebral cortex' | 0.01032 | 0.00481 | 0.00452 | 0.00550 | 0.01398 | 0.01145 | 0.01035 | 0.00472 | 0.00597 | 0.00237 | 0.00620 | 0.00811 | 0.00304 | 0.00172 | 0.00518 | 0.0750 | 0.0952 | 0.0972 | 0.9817 | 0.0322 | 0.0425 | 0.8619 | 1 |
| Mop | 'Primary motor area' | 0.00270 | 0.00183 | 0.00089 | 0.00226 | 0.00214 | 0.00258 | 0.00381 | 0.00126 | 0.00206 | 0.00156 | 0.00245 | 0.00067 | 0.00061 | 0.00105 | 0.00123 | 0.0229 | 0.2381 | 0.0266 | 0.0621 | 0.1111 | 0.0045 | 0.0208 | 1 |
| Mos | 'Secondary motor area' | 0.00556 | 0.00388 | 0.00251 | 0.00354 | 0.00541 | 0.00534 | 0.00795 | 0.00382 | 0.00534 | 0.00194 | 0.00442 | 0.00146 | 0.00268 | 0.00309 | 0.00281 | 0.0405 | 0.3783 | 0.0757 | 0.301 | 0.1967 | 0.0206 | 0.1393 | 1 |
| SSp | 'Primary somatosensory area' | 0.00254 | 0.00190 | 0.00076 | 0.00277 | 0.00102 | 0.00261 | 0.00375 | 0.00098 | 0.00168 | 0.00220 | 0.00275 | 0.00060 | 0.00067 | 0.00089 | 0.00089 | 0.0215 | 0.6433 | 0.0996 | 0.1073 | 0.3865 | 0.0210 | 0.0252 | 1 |
| SSs | 'Supplemental somatosensory area' | 0.00479 | 0.00343 | 0.00053 | 0.00300 | 0.00422 | 0.00544 | 0.00649 | 0.00192 | 0.00352 | 0.00397 | 0.00431 | 0.00062 | 0.00030 | 0.00039 | 0.00080 | 0.0540 | 0.3732 | 0.0207 | 0.0209 | 0.1907 | 0.0014 | 0.0017 | 1 |
| GU | 'Gustatory areas' | 0.00683 | 0.00435 | 0.00079 | 0.00219 | 0.00935 | 0.00894 | 0.00685 | 0.00271 | 0.00613 | 0.00372 | 0.00483 | 0.00097 | 0.00012 | 0.00168 | 0.00038 | 0.0814 | 0.4279 | 0.0646 | 0.0225 | 0.2158 | 0.0113 | 0.0047 | 1 |
| VISC | 'Visceral area' | 0.00900 | 0.00577 | 0.00056 | 0.00418 | 0.01124 | 0.01248 | 0.00811 | 0.00324 | 0.00819 | 0.00579 | 0.00586 | 0.00072 | 0.00010 | 0.00055 | 0.00086 | 0.1073 | 0.3588 | 0.039 | 0.0265 | 0.1766 | 0.0039 | 0.0022 | 1 |
| AUDd | 'Dorsal auditory area' | 0.00916 | 0.00652 | 0.00162 | 0.00851 | 0.00647 | 0.00846 | 0.01319 | 0.00418 | 0.00415 | 0.00753 | 0.01021 | 0.00134 | 0.00109 | 0.00136 | 0.00269 | 0.0918 | 0.4494 | 0.0222 | 0.0818 | 0.2436 | 0.0022 | 0.0176 | 1 |
| AUDp | 'Primary auditory area' | 0.00639 | 0.00440 | 0.00098 | 0.00652 | 0.00552 | 0.00597 | 0.00753 | 0.00309 | 0.00302 | 0.00505 | 0.00644 | 0.00076 | 0.00029 | 0.00109 | 0.00177 | 0.0640 | 0.1875 | 0.0002 | 0.0412 | 0.0771 | 0.0001 | 0.0082 | 1 |
| AUDpo | 'Posterior auditory area' | 0.01004 | 0.00598 | 0.00236 | 0.01315 | 0.00414 | 0.01124 | 0.01164 | 0.00384 | 0.00275 | 0.00613 | 0.01120 | 0.00233 | 0.00119 | 0.00259 | 0.00332 | 0.0887 | 0.3652 | 0.0582 | 0.2769 | 0.1902 | 0.0097 | 0.1090 | 1 |
| AUDv | 'Ventral auditory area' | 0.00967 | 0.00685 | 0.00064 | 0.00631 | 0.01255 | 0.00966 | 0.01015 | 0.00582 | 0.00769 | 0.00742 | 0.00646 | 0.00072 | 0.00018 | 0.00062 | 0.00105 | 0.1091 | 0.2182 | 0.0111 | 0.0004 | 0.0828 | 0.0004 | 0.0000 | 1 |
| VISal | 'Anterolateral visual area' | 0.00698 | 0.00444 | 0.00280 | 0.01018 | 0.00179 | 0.00790 | 0.00806 | 0.00296 | 0.00280 | 0.00551 | 0.00649 | 0.00184 | 0.00164 | 0.00326 | 0.00445 | 0.0438 | 0.4822 | 0.1953 | 0.3828 | 0.2570 | 0.0724 | 0.1975 | 1 |
| VISam | 'Anteromedial visual area' | 0.01042 | 0.00439 | 0.00541 | 0.01345 | 0.00328 | 0.01371 | 0.01123 | 0.00234 | 0.00526 | 0.00283 | 0.00714 | 0.00497 | 0.00742 | 0.00462 | 0.00461 | 0.0523 | 0.172 | 0.2481 | 0.7329 | 0.0660 | 0.0954 | 0.4668 | 1 |
| VISl | 'Lateral visual area' | 0.00532 | 0.00276 | 0.00183 | 0.00720 | 0.00250 | 0.00539 | 0.00618 | 0.00231 | 0.00197 | 0.00359 | 0.00317 | 0.00161 | 0.00087 | 0.00231 | 0.00255 | 0.0363 | 0.1594 | 0.0711 | 0.2677 | 0.0555 | 0.0180 | 0.1324 | 1 |
| VISp | 'Primary visual area' | 0.00655 | 0.00255 | 0.00152 | 0.00887 | 0.00527 | 0.00681 | 0.00526 | 0.00160 | 0.00126 | 0.00361 | 0.00371 | 0.00106 | 0.00151 | 0.00171 | 0.00179 | 0.0515 | 0.0252 | 0.0174 | 0.3816 | 0.0097 | 0.0012 | 0.1751 | 1 |
| VISpl | 'Posterolateral visual area' | 0.01018 | 0.00620 | 0.00227 | 0.00974 | 0.01249 | 0.01301 | 0.00547 | 0.00570 | 0.00196 | 0.00632 | 0.01083 | 0.00163 | 0.00059 | 0.00504 | 0.00180 | 0.0976 | 0.3215 | 0.026 | 0.237 | 0.1640 | 0.0071 | 0.1043 | 1 |
| VISpm | 'posteromedial visual area' | 0.01562 | 0.00630 | 0.00488 | 0.01909 | 0.01145 | 0.01953 | 0.01241 | 0.00397 | 0.00621 | 0.00591 | 0.00909 | 0.00429 | 0.00563 | 0.00332 | 0.00628 | 0.1124 | 0.0322 | 0.0243 | 0.536 | 0.0079 | 0.0030 | 0.2997 | 1 |
| ACC | 'Anterior cingulate area' | 0.00889 | 0.00599 | 0.00649 | 0.00911 | 0.00832 | 0.00942 | 0.00870 | 0.00424 | 0.00662 | 0.00517 | 0.00794 | 0.00502 | 0.00827 | 0.00756 | 0.00512 | 0.0288 | 0.0676 | 0.1188 | 0.905 | 0.0142 | 0.0330 | 0.6832 | 2 |
| PL | 'Prelimbic area' | 0.00833 | 0.00361 | 0.00626 | 0.00983 | 0.00911 | 0.00500 | 0.00939 | 0.00386 | 0.00286 | 0.00276 | 0.00497 | 0.00538 | 0.00474 | 0.01011 | 0.00481 | 0.0248 | 0.0367 | 0.4899 | 0.2532 | 0.0087 | 0.2706 | 0.1059 | 2 |
| IL | 'Infralimbic area' | 0.00730 | 0.00156 | 0.00871 | 0.00833 | 0.00387 | 0.00315 | 0.01387 | 0.00083 | 0.00437 | 0.00073 | 0.00031 | 0.00462 | 0.00568 | 0.01835 | 0.00621 | -0.0088 | 0.1939 | 0.9366 | 0.2132 | 0.0728 | 0.7404 | 0.0775 | 2 |
| ORBl | 'Orbital area, lateral part' | 0.00185 | 0.00101 | 0.00220 | 0.00122 | 0.00213 | 0.00168 | 0.00236 | 0.00099 | 0.00088 | 0.00126 | 0.00092 | 0.00160 | 0.00156 | 0.00317 | 0.00248 | -0.0027 | 0.081 | 0.7356 | 0.1016 | 0.0206 | 0.4717 | 0.0236 | 1 |
| ORBm | 'Orbital area, medial part' | 0.00432 | 0.00196 | 0.00734 | 0.00086 | 0.00794 | 0.00508 | 0.00342 | 0.00176 | 0.00550 | 0.00018 | 0.00041 | 0.00792 | 0.00531 | 0.00958 | 0.00653 | -0.0257 | 0.4838 | 0.2851 | 0.0332 | 0.2668 | 0.1350 | 0.0128 | 1 |
| ORBvl | 'Orbital area, ventrolateral part' | 0.00152 | 0.00066 | 0.00234 | 0.00074 | 0.00237 | 0.00175 | 0.00121 | 0.00021 | 0.00141 | 0.00017 | 0.00086 | 0.00152 | 0.00154 | 0.00505 | 0.00126 | -0.0041 | 0.231 | 0.6965 | 0.2998 | 0.1115 | 0.4275 | 0.1276 | 1 |
| AId | 'Agranular insular area, dorsal part' | 0.00911 | 0.00647 | 0.00565 | 0.00561 | 0.01027 | 0.01129 | 0.00925 | 0.00657 | 0.00598 | 0.00692 | 0.00642 | 0.00661 | 0.00183 | 0.00714 | 0.00703 | 0.0490 | 0.2307 | 0.2082 | 0.8131 | 0.0800 | 0.1001 | 0.5490 | 1 |
| AIp | 'Agranular insular area, posterior part' | 0.01245 | 0.00844 | 0.00136 | 0.00639 | 0.01595 | 0.01851 | 0.00894 | 0.00798 | 0.00965 | 0.00818 | 0.00795 | 0.00144 | 0.00028 | 0.00250 | 0.00121 | 0.1394 | 0.4458 | 0.0579 | 0.0001 | 0.2141 | 0.0086 | 0.0000 | 1 |
| AIv | 'Agranular insular area, ventral part' | 0.01792 | 0.00801 | 0.00869 | 0.01654 | 0.01733 | 0.01863 | 0.01918 | 0.00803 | 0.01064 | 0.00506 | 0.00831 | 0.01009 | 0.00459 | 0.00738 | 0.01269 | 0.1059 | 0.0021 | 0.0195 | 0.9441 | 0.0003 | 0.0024 | 0.7573 | 1 |
| RSP | 'Retrosplenial area' | 0.01266 | 0.00652 | 0.00656 | 0.01183 | 0.01119 | 0.01794 | 0.00969 | 0.00442 | 0.00631 | 0.00630 | 0.00907 | 0.00556 | 0.00702 | 0.00622 | 0.00742 | 0.0702 | 0.0735 | 0.0812 | 0.9995 | 0.0243 | 0.0169 | 0.9769 | 1 |
| VISrl | 'Rostrolateral visual area' | 0.01076 | 0.00761 | 0.00122 | 0.01044 | 0.00882 | 0.01256 | 0.01123 | 0.00955 | 0.00592 | 0.00620 | 0.00879 | 0.00073 | 0.00115 | 0.00075 | 0.00223 | 0.1092 | 0.0893 | 0.0007 | 0.0069 | 0.0395 | 0.0000 | 0.0006 | 1 |
| TEa | 'Temporal association areas' | 0.01926 | 0.01368 | 0.00171 | 0.01369 | 0.01957 | 0.02109 | 0.02271 | 0.01250 | 0.01669 | 0.01120 | 0.01431 | 0.00205 | 0.00051 | 0.00222 | 0.00207 | 0.2168 | 0.1263 | 0.0048 | 0.0022 | 0.0509 | 0.0001 | 0.0001 | 1 |
| PERI | 'Perirhinal area' | 0.02741 | 0.02306 | 0.00318 | 0.02034 | 0.03022 | 0.03142 | 0.02765 | 0.02414 | 0.02394 | 0.01485 | 0.02934 | 0.00337 | 0.00139 | 0.00415 | 0.00378 | 0.3069 | 0.543 | 0.0032 | 0.0121 | 0.3086 | 0.0001 | 0.0006 | 1 |
| ECT | 'Ectorhinal area' | 0.03475 | 0.02265 | 0.00307 | 0.02323 | 0.04236 | 0.03622 | 0.03828 | 0.02182 | 0.02649 | 0.01640 | 0.02591 | 0.00377 | 0.00138 | 0.00435 | 0.00277 | 0.3937 | 0.1031 | 0.0074 | 0.0048 | 0.0393 | 0.0002 | 0.0002 | 1 |
| OLF | 'Olfactory areas' | 0.00543 | 0.00473 | 0.00557 | 0.00392 | 0.00521 | 0.00729 | 0.00528 | 0.00543 | 0.00630 | 0.00283 | 0.00435 | 0.00697 | 0.00257 | 0.00841 | 0.00431 | 0.0089 | 0.7817 | 0.9951 | 0.8488 | 0.5184 | 0.9282 | 0.5981 | 1 |
| AOB | 'Accessory olfactory bulb' | 0.00145 | 0.00150 | 0.00189 | 0.00261 | 0.00083 | 0.00182 | 0.00054 | 0.00141 | 0.00143 | 0.00134 | 0.00180 | 0.00132 | 0.00113 | 0.00338 | 0.00174 | -0.0048 | 0.9953 | 0.8076 | 0.7475 | 0.9250 | 0.5490 | 0.4784 | 1 |
| AON | 'Anterior olfactory nucleus' | 0.00507 | 0.00369 | 0.00619 | 0.00399 | 0.00493 | 0.00748 | 0.00389 | 0.00267 | 0.00625 | 0.00184 | 0.00399 | 0.00709 | 0.00117 | 0.01145 | 0.00244 | 0.0020 | 0.5561 | 0.8749 | 0.5615 | 0.3183 | 0.6351 | 0.3144 | 1 |
| TT | 'Taenia tecta' | 0.01730 | 0.01019 | 0.01122 | 0.01100 | 0.02088 | 0.02117 | 0.01679 | 0.01140 | 0.01399 | 0.01452 | 0.00987 | 0.01359 | 0.00646 | 0.01230 | 0.01054 | 0.0929 | 0.281 | 0.1877 | 0.9626 | 0.1352 | 0.0882 | 0.8004 | 1 |
| DP | 'Dorsal peduncular area' | 0.00404 | 0.00327 | 0.01098 | 0.00374 | 0.00450 | 0.00410 | 0.00382 | 0.00370 | 0.00606 | 0.00169 | 0.00162 | 0.01197 | 0.00211 | 0.02059 | 0.00924 | -0.0614 | 0.7655 | 0.3051 | 0.2557 | 0.4951 | 0.1194 | 0.0995 | 2 |
| PIR | 'Piriform area' | 0.00391 | 0.00785 | 0.00318 | 0.00270 | 0.00337 | 0.00574 | 0.00380 | 0.00782 | 0.00455 | 0.00889 | 0.01017 | 0.00261 | 0.00031 | 0.00545 | 0.00435 | 0.0196 | 0.0803 | 0.8479 | 0.0663 | 0.0279 | 0.5954 | 0.0294 | 1 |
| NLOT | 'Nucleus of the lateral olfactory tract' | 0.01308 | 0.01788 | 0.02135 | 0.00846 | 0.01715 | 0.01303 | 0.01365 | 0.01838 | 0.01471 | 0.01458 | 0.02387 | 0.02413 | 0.00929 | 0.03616 | 0.01582 | -0.0444 | 0.2801 | 0.4455 | 0.8478 | 0.1388 | 0.2213 | 0.5956 | 1 |
| COAa | 'Cortical amygdalar area, anterior part' | 0.00976 | 0.02289 | 0.02058 | 0.00732 | 0.01161 | 0.01186 | 0.00826 | 0.02531 | 0.02412 | 0.01576 | 0.02636 | 0.02079 | 0.00931 | 0.03453 | 0.01768 | -0.0757 | 0.0148 | 0.2449 | 0.9173 | 0.0027 | 0.0907 | 0.7031 | 1 |
| COAp | 'Cortical amygdalar area, posterior part' | 0.00503 | 0.00796 | 0.00482 | 0.00246 | 0.00561 | 0.00434 | 0.00770 | 0.00961 | 0.00625 | 0.00848 | 0.00751 | 0.00340 | 0.00350 | 0.00694 | 0.00544 | 0.0104 | 0.1549 | 0.9878 | 0.0687 | 0.0669 | 0.8854 | 0.0298 | 1 |
| PAA | 'Piriform-amygdalar area' | 0.00468 | 0.01235 | 0.00570 | 0.00236 | 0.00505 | 0.00452 | 0.00678 | 0.01221 | 0.01153 | 0.01111 | 0.01453 | 0.00945 | 0.00027 | 0.00786 | 0.00520 | 0.0121 | 0.0018 | 0.8922 | 0.0798 | 0.0007 | 0.6603 | 0.0213 | 1 |
| TR | 'Postpiriform transition area' | 0.00106 | 0.00379 | 0.00174 | 0.00049 | 0.00222 | 0.00088 | 0.00064 | 0.00292 | 0.00079 | 0.00542 | 0.00600 | 0.00079 | 0.00028 | 0.00326 | 0.00262 | -0.0016 | 0.2033 | 0.7021 | 0.3827 | 0.0741 | 0.4350 | 0.1933 | 1 |
| HPF | 'Hippocampal formation' | 0.00256 | 0.00205 | 0.00135 | 0.00310 | 0.00389 | 0.00198 | 0.00128 | 0.00178 | 0.00076 | 0.00294 | 0.00273 | 0.00125 | 0.00057 | 0.00280 | 0.00078 | 0.0147 | 0.7906 | 0.3253 | 0.6089 | 0.5287 | 0.1646 | 0.3598 | 2 |
| CA1 | 'Field CA1' | 0.00026 | 0.00039 | 0.00012 | 0.00042 | 0.00033 | 0.00006 | 0.00021 | 0.00017 | 0.00007 | 0.00082 | 0.00050 | 0.00003 | 0.00012 | 0.00017 | 0.00016 | 0.0012 | 0.7647 | 0.3444 | 0.3788 | 0.4916 | 0.1609 | 0.1647 | 2 |
| CA2 | 'Field CA2' | 0.00012 | 0.00011 | 0.00007 | 0.00019 | 0.00015 | 0.00002 | 0.00011 | 0.00003 | 0.00002 | 0.00023 | 0.00016 | 0.00002 | 0.00013 | 0.00007 | 0.00006 | 0.0003 | 0.9922 | 0.5502 | 0.7683 | 0.9263 | 0.3421 | 0.5105 | 2 |
| CA3 | 'Field CA3' | 0.00048 | 0.00052 | 0.00038 | 0.00066 | 0.00053 | 0.00047 | 0.00025 | 0.00036 | 0.00015 | 0.00081 | 0.00078 | 0.00088 | 0.00026 | 0.00034 | 0.00003 | 0.0014 | 0.9638 | 0.8742 | 0.8204 | 0.8056 | 0.6463 | 0.5767 | 2 |
| DG | 'Dentate gyrus' | 0.00054 | 0.00063 | 0.00035 | 0.00068 | 0.00089 | 0.00037 | 0.00021 | 0.00054 | 0.00026 | 0.00070 | 0.00101 | 0.00062 | 0.00028 | 0.00028 | 0.00023 | 0.0024 | 0.9122 | 0.5854 | 0.3604 | 0.7123 | 0.3273 | 0.1795 | 2 |
| ENTl | 'Entorhinal area, lateral part' | 0.01786 | 0.01652 | 0.00298 | 0.01434 | 0.02296 | 0.01590 | 0.01826 | 0.01573 | 0.01002 | 0.01589 | 0.02442 | 0.00223 | 0.00049 | 0.00434 | 0.00485 | 0.1888 | 0.923 | 0.003 | 0.0315 | 0.7149 | 0.0004 | 0.0050 | 1 |
| ENTm | 'Entorhinal area, medial part, dorsal zone' | 0.00444 | 0.00550 | 0.00109 | 0.00245 | 0.00550 | 0.00387 | 0.00593 | 0.00631 | 0.00308 | 0.00587 | 0.00675 | 0.00052 | 0.00016 | 0.00186 | 0.00184 | 0.0448 | 0.6447 | 0.036 | 0.0149 | 0.3907 | 0.0105 | 0.0033 | 1 |
| PAR | 'Parasubiculum' | 0.00360 | 0.00230 | 0.00057 | 0.00434 | 0.00602 | 0.00276 | 0.00128 | 0.00174 | 0.00020 | 0.00260 | 0.00466 | 0.00048 | 0.00034 | 0.00036 | 0.00111 | 0.0338 | 0.6366 | 0.1127 | 0.2953 | 0.3829 | 0.0265 | 0.1174 | 1 |
| POST | 'Postsubiculum' | 0.00526 | 0.00162 | 0.00101 | 0.00742 | 0.00633 | 0.00504 | 0.00225 | 0.00138 | 0.00056 | 0.00201 | 0.00252 | 0.00130 | 0.00096 | 0.00148 | 0.00029 | 0.0433 | 0.0828 | 0.058 | 0.4896 | 0.0224 | 0.0099 | 0.2659 | 1 |
| PRE | 'Presubiculum' | 0.00332 | 0.00244 | 0.00085 | 0.00546 | 0.00298 | 0.00362 | 0.00122 | 0.00177 | 0.00047 | 0.00221 | 0.00530 | 0.00089 | 0.00086 | 0.00134 | 0.00032 | 0.0278 | 0.7965 | 0.1255 | 0.3924 | 0.5353 | 0.0337 | 0.1804 | 1 |
| SUB | 'Subiculum' | 0.00191 | 0.00097 | 0.00025 | 0.00383 | 0.00191 | 0.00170 | 0.00018 | 0.00034 | 0.00016 | 0.00073 | 0.00265 | 0.00024 | 0.00018 | 0.00044 | 0.00016 | 0.0170 | 0.6095 | 0.216 | 0.5095 | 0.3579 | 0.0701 | 0.2605 | 1 |
| CTXsp | 'Cortical subplate' | 0.00645 | 0.00733 | 0.00430 | 0.00529 | 0.00467 | 0.00631 | 0.00954 | 0.00627 | 0.00576 | 0.00944 | 0.00786 | 0.00518 | 0.00232 | 0.00624 | 0.00347 | 0.0332 | 0.8028 | 0.3397 | 0.1008 | 0.5438 | 0.1733 | 0.0458 | 2 |
| CLA | 'Claustrum' | 0.02057 | 0.01108 | 0.00573 | 0.01686 | 0.02129 | 0.02119 | 0.02294 | 0.00904 | 0.01206 | 0.00999 | 0.01322 | 0.00765 | 0.00328 | 0.00865 | 0.00333 | 0.1849 | 0.0034 | 0.0006 | 0.0534 | 0.0011 | 0.0002 | 0.0202 | 2 |
| EP | 'Endopiriform nucleus' | 0.01060 | 0.00856 | 0.00404 | 0.00481 | 0.00830 | 0.01422 | 0.01505 | 0.00892 | 0.00751 | 0.00953 | 0.00830 | 0.00462 | 0.00056 | 0.00656 | 0.00441 | 0.0919 | 0.7182 | 0.1418 | 0.0636 | 0.4444 | 0.0543 | 0.0144 | 1 |
| LA | 'Lateral amygdalar nucleus' | 0.00465 | 0.00539 | 0.00119 | 0.00299 | 0.00298 | 0.00463 | 0.00799 | 0.00229 | 0.00483 | 0.00883 | 0.00559 | 0.00151 | 0.00085 | 0.00168 | 0.00071 | 0.0460 | 0.9121 | 0.1152 | 0.1004 | 0.6943 | 0.0284 | 0.0220 | 2 |
| BLAa | 'Basolateral amygdalar nucleus, anterior part | 0.01635 | 0.01832 | 0.00516 | 0.01210 | 0.01462 | 0.01916 | 0.01953 | 0.01445 | 0.02162 | 0.01771 | 0.01948 | 0.00635 | 0.00491 | 0.00623 | 0.00316 | 0.1496 | 0.6986 | 0.0101 | 0.0023 | 0.4371 | 0.0012 | 0.0002 | 2 |
| BLAp | 'Basolateral amygdalar nucleus, posterior pa | 0.00540 | 0.00750 | 0.00335 | 0.00379 | 0.00745 | 0.00476 | 0.00561 | 0.00448 | 0.00739 | 0.00930 | 0.00883 | 0.00353 | 0.00182 | 0.00558 | 0.00246 | 0.0351 | 0.3332 | 0.2435 | 0.0553 | 0.1669 | 0.1192 | 0.0226 | 2 |
| BLAv | 'Basolateral amygdalar nucleus, ventral part' | 0.01065 | 0.01646 | 0.01265 | 0.00657 | 0.00923 | 0.01543 | 0.01139 | 0.01277 | 0.01343 | 0.01600 | 0.02362 | 0.01502 | 0.00292 | 0.02161 | 0.01106 | 0.0211 | 0.2346 | 0.8922 | 0.7073 | 0.1117 | 0.6612 | 0.4426 | 1 |
| BMAa | 'Basomedial amygdalar nucleus, anterior par | 0.00816 | 0.01107 | 0.01350 | 0.00589 | 0.00710 | 0.00999 | 0.00966 | 0.00938 | 0.01257 | 0.00991 | 0.01242 | 0.01271 | 0.01005 | 0.01892 | 0.01231 | -0.0416 | 0.1435 | 0.1259 | 0.5264 | 0.0658 | 0.0472 | 0.2858 | 1 |
| BMAp | 'Basomedial amygdalar nucleus, posterior pa | 0.00906 | 0.00909 | 0.00746 | 0.00613 | 0.00862 | 0.00913 | 0.01239 | 0.01112 | 0.00547 | 0.01071 | 0.00907 | 0.00457 | 0.00744 | 0.00837 | 0.00944 | 0.0203 | 0.9999 | 0.6197 | 0.6111 | 0.9877 | 0.3695 | 0.3612 | 1 |
| PA | 'Posterior amygdalar nucleus' | 0.00341 | 0.00423 | 0.00281 | 0.00257 | 0.00253 | 0.00366 | 0.00490 | 0.00476 | 0.00295 | 0.00488 | 0.00344 | 0.00058 | 0.00292 | 0.00285 | 0.00085 | 0.0077 | 0.6753 | 0.8348 | 0.477 | 0.4148 | 0.5814 | 0.2619 | 1 |
| STR | 'Striatum' | 0.00418 | 0.00384 | 0.00478 | 0.00291 | 0.00416 | 0.00410 | 0.00554 | 0.00333 | 0.00570 | 0.00321 | 0.00313 | 0.00560 | 0.00390 | 0.00619 | 0.00343 | -0.0007 | 0.9136 | 0.7691 | 0.585 | 0.6993 | 0.5046 | 0.3412 | 2 |
| CP | 'Caudoputamen' | 0.00751 | 0.00468 | 0.00356 | 0.00565 | 0.00384 | 0.00568 | 0.01487 | 0.00196 | 0.00376 | 0.00918 | 0.00383 | 0.00330 | 0.00504 | 0.00261 | 0.00330 | 0.0441 | 0.629 | 0.3799 | 0.7873 | 0.3728 | 0.1715 | 0.5223 | 3 |
| STRv | 'Striatum ventral region' | 0.00222 | 0.00370 | 0.00421 | 0.00216 | 0.00152 | 0.00197 | 0.00325 | 0.00318 | 0.00354 | 0.00462 | 0.00346 | 0.00505 | 0.00256 | 0.00628 | 0.00294 | -0.0171 | 0.0527 | 0.21 | 0.8563 | 0.0226 | 0.0830 | 0.6076 | 2 |
| NAc | 'Nucleus accumbens' | 0.03172 | 0.01904 | 0.01628 | 0.02104 | 0.02803 | 0.02880 | 0.04209 | 0.01726 | 0.03056 | 0.01164 | 0.01670 | 0.01852 | 0.00857 | 0.02228 | 0.01577 | 0.2146 | 0.2737 | 0.1578 | 0.8488 | 0.1312 | 0.0604 | 0.5993 | 3 |
| OT | 'Olfactory tubercle' | 0.01534 | 0.01624 | 0.01574 | 0.00947 | 0.01682 | 0.02063 | 0.01442 | 0.01926 | 0.01738 | 0.01047 | 0.01786 | 0.02075 | 0.00659 | 0.02357 | 0.01205 | 0.0330 | 0.9528 | 0.9957 | 0.9928 | 0.7767 | 0.9325 | 0.9123 | 1 |
| LSx | 'Lateral septal complex' | 0.00467 | 0.00483 | 0.00858 | 0.00587 | 0.00367 | 0.00165 | 0.00749 | 0.00373 | 0.00672 | 0.00422 | 0.00465 | 0.00972 | 0.00526 | 0.00719 | 0.01214 | -0.0459 | 0.9932 | 0.1982 | 0.1655 | 0.9145 | 0.0943 | 0.0620 | 3 |
| sAMY | 'Striatum-like amygdalar nuclei' | 0.00878 | 0.01287 | 0.01276 | 0.00685 | 0.01106 | 0.00700 | 0.01020 | 0.01122 | 0.01304 | 0.01276 | 0.01447 | 0.01850 | 0.00835 | 0.01552 | 0.00868 | -0.0243 | 0.0522 | 0.4012 | 0.999 | 0.0182 | 0.1975 | 0.9690 | 2 |
| CEA | 'Central amygdalar nucleus' | 0.00197 | 0.00215 | 0.00389 | 0.00130 | 0.00107 | 0.00092 | 0.00459 | 0.00129 | 0.00243 | 0.00350 | 0.00137 | 0.00358 | 0.00250 | 0.00733 | 0.00216 | -0.0158 | 0.9835 | 0.4472 | 0.4431 | 0.8637 | 0.2394 | 0.2270 | 2 |
| MEA | 'Medial amygdalar nucleus' | 0.00868 | 0.00360 | 0.01262 | 0.00633 | 0.01050 | 0.00981 | 0.00808 | 0.01671 | 0.01585 | 0.01011 | 0.01172 | 0.00979 | 0.01287 | 0.01485 | 0.01298 | -0.0381 | 0.0986 | 0.0699 | 0.8692 | 0.0374 | 0.0308 | 0.6283 | 1 |
| PAL | 'Pallidum' | 0.00643 | 0.00651 | 0.00757 | 0.00573 | 0.00617 | 0.00599 | 0.00785 | 0.00522 | 0.00925 | 0.00504 | 0.00654 | 0.00671 | 0.00072 | 0.00634 | 0.00650 | -0.0130 | 0.9972 | 0.6253 | 0.7526 | 0.9657 | 0.3649 | 0.4885 | 3 |
| GPe | 'Globus pallidus, external segment' | 0.00108 | 0.00103 | 0.00191 | 0.00116 | 0.00021 | 0.00027 | 0.00267 | 0.00083 | 0.00047 | 0.00255 | 0.00025 | 0.00136 | 0.00364 | 0.00094 | 0.00170 | -0.0142 | 0.9975 | 0.6005 | 0.5405 | 0.9490 | 0.3551 | 0.3092 | 3 |
| GPi | 'Globus pallidus, internal segment' | 0.00179 | 0.00205 | 0.00380 | 0.00232 | 0.00091 | 0.00059 | 0.00334 | 0.00130 | 0.00372 | 0.00238 | 0.00079 | 0.00351 | 0.00642 | 0.00119 | 0.00409 | -0.0302 | 0.9572 | 0.3259 | 0.4099 | 0.7857 | 0.1586 | 0.2122 | 3 |
| SI | 'Substantia innominata' | 0.00666 | 0.00669 | 0.00983 | 0.00458 | 0.00864 | 0.00638 | 0.00705 | 0.00519 | 0.01064 | 0.00459 | 0.00636 | 0.01099 | 0.00622 | 0.01407 | 0.00802 | -0.0206 | 0.9998 | 0.3209 | 0.3908 | 0.9851 | 0.1498 | 0.2040 | 2 |
| MA | 'Magnocellular nucleus' | 0.00934 | 0.00964 | 0.01713 | 0.00694 | 0.01143 | 0.00837 | 0.01061 | 0.00586 | 0.01698 | 0.00592 | 0.00979 | 0.01817 | 0.00789 | 0.02403 | 0.01845 | -0.0636 | 0.9937 | 0.1941 | 0.2645 | 0.9187 | 0.0684 | 0.1288 | 1 |
| MS | 'Medial septal nucleus' | 0.01031 | 0.01251 | 0.01892 | 0.01269 | 0.00925 | 0.00371 | 0.01559 | 0.01471 | 0.01134 | 0.01094 | 0.01307 | 0.02035 | 0.00879 | 0.02416 | 0.02238 | -0.0888 | 0.7149 | 0.1992 | 0.299 | 0.4451 | 0.0925 | 0.1232 | 3 |
| NDB | 'Diagonal band nucleus' | 0.02438 | 0.01392 | 0.01706 | 0.01910 | 0.02705 | 0.03107 | 0.02028 | 0.01546 | 0.02259 | 0.00757 | 0.01005 | 0.02147 | 0.02375 | 0.01704 | 0.00596 | 0.0895 | 0.119 | 0.3593 | 0.8217 | 0.0539 | 0.1830 | 0.5659 | 1 |
| TRS | 'Triangular nucleus of septum' | 0.00607 | 0.00625 | 0.01072 | 0.00810 | 0.00415 | 0.00150 | 0.01053 | 0.00307 | 0.00546 | 0.00827 | 0.00820 | 0.01588 | 0.00777 | 0.00570 | 0.01352 | -0.0564 | 0.9968 | 0.3617 | 0.3145 | 0.9422 | 0.1870 | 0.1479 | 3 |
| BST | 'Bed nuclei of the stria terminalis' | 0.00482 | 0.00590 | 0.00980 | 0.00419 | 0.00247 | 0.00267 | 0.00996 | 0.00456 | 0.01223 | 0.00434 | 0.00248 | 0.00518 | 0.01031 | 0.00937 | 0.01433 | -0.0609 | 0.9214 | 0.2096 | 0.4174 | 0.7110 | 0.1010 | 0.2227 | 3 |
| TH | 'Thalamus' | 0.00416 | 0.00595 | 0.00981 | 0.00589 | 0.00395 | 0.00315 | 0.00367 | 0.00661 | 0.00581 | 0.00725 | 0.00415 | 0.00667 | 0.01578 | 0.00532 | 0.01147 | -0.0840 | 0.1956 | 0.1862 | 0.3734 | 0.0934 | 0.0615 | 0.1708 | 3 |
| VENT | 'Ventral group of the dorsal thalamus' | 0.00135 | 0.00111 | 0.00403 | 0.00271 | 0.00351 | 0.00079 | 0.00159 | 0.00126 | 0.00111 | 0.00158 | 0.00047 | 0.00037 | 0.01055 | 0.00037 | 0.00484 | -0.0472 | 0.9067 | 0.5792 | 0.5254 | 0.6873 | 0.3192 | 0.2731 | 3 |
| SPF | 'Subparafascicular nucleus' | 0.00283 | 0.00297 | 0.00909 | 0.00384 | 0.00222 | 0.00241 | 0.00285 | 0.00522 | 0.00247 | 0.00373 | 0.00045 | 0.00024 | 0.02081 | 0.00267 | 0.01265 | -0.1037 | 0.991 | 0.4772 | 0.4953 | 0.9014 | 0.2361 | 0.2536 | 3 |
| SPA | 'Subparafascicular area' | 0.00574 | 0.00990 | 0.01948 | 0.00167 | 0.00213 | 0.01133 | 0.00782 | 0.02195 | 0.00855 | 0.00663 | 0.00248 | 0.00296 | 0.02732 | 0.01384 | 0.03379 | -0.1912 | 0.6841 | 0.2643 | 0.5108 | 0.4201 | 0.1081 | 0.2808 | 3 |
| PP | 'Peripeduncular nucleus' | 0.00696 | 0.00961 | 0.01347 | 0.01080 | 0.00767 | 0.00420 | 0.00517 | 0.00421 | 0.00385 | 0.01514 | 0.01523 | 0.01155 | 0.01349 | 0.01612 | 0.01273 | -0.0747 | 0.7505 | 0.0299 | 0.5444 | 0.4837 | 0.0103 | 0.2944 | 3 |
| GENd | 'Geniculate group, dorsal thalamus' | 0.00754 | 0.00406 | 0.00352 | 0.01348 | 0.00544 | 0.00432 | 0.00694 | 0.00024 | 0.00006 | 0.01096 | 0.00499 | 0.00325 | 0.00809 | 0.00136 | 0.00139 | 0.0249 | 0.5715 | 0.3381 | 0.9826 | 0.3301 | 0.1712 | 0.8626 | 3 |
| LAT | 'Lateral group of the dorsal thalamus' | 0.00148 | 0.00214 | 0.00282 | 0.00294 | 0.00131 | 0.00077 | 0.00090 | 0.00131 | 0.00126 | 0.00401 | 0.00200 | 0.00339 | 0.00438 | 0.00166 | 0.00184 | -0.0209 | 0.7088 | 0.3084 | 

| | | | | | | | | | | | | | | | | | | | | | | |
|---|---|---|---|---|---|---|---|---|---|---|---|---|---|---|---|---|---|---|---|---|---|---|
| AHN | 'Anterior hypothalamic nucleus' | 0.01526 | 0.01678 | 0.01698 | 0.02051 | 0.01631 | 0.01564 | 0.00859 | 0.02385 | 0.01946 | 0.01383 | 0.00996 | 0.02004 | 0.02256 | 0.01167 | 0.01362 | -0.0472 | 0.9228 | 0.8838 | 0.9987 | 0.7134 | 0.6484 | 0.9618 | 1 |
| MBO | 'Mammillary body' | 0.01285 | 0.01370 | 0.01591 | 0.01407 | 0.01684 | 0.01336 | 0.00712 | 0.02143 | 0.01526 | 0.01090 | 0.00722 | 0.01416 | 0.02398 | 0.01368 | 0.01182 | -0.0573 | 0.9708 | 0.664 | 0.8561 | 0.8240 | 0.4049 | 0.6097 | 1 |
| MPN | 'Medial preoptic nucleus' | 0.00810 | 0.01465 | 0.01282 | 0.00795 | 0.00949 | 0.00981 | 0.00515 | 0.02361 | 0.01476 | 0.01080 | 0.00941 | 0.00784 | 0.01875 | 0.01006 | 0.01464 | -0.0707 | 0.2505 | 0.2839 | 0.8947 | 0.0997 | 0.1251 | 0.6656 | 1 |
| PMd | 'Dorsal premammillary nucleus' | 0.01371 | 0.01921 | 0.01581 | 0.01097 | 0.01499 | 0.01536 | 0.01351 | 0.03642 | 0.02678 | 0.01017 | 0.00346 | 0.01256 | 0.02410 | 0.00599 | 0.02061 | -0.0582 | 0.7682 | 0.8747 | 0.9188 | 0.4972 | 0.6332 | 0.7060 | 1 |
| PMv | 'Ventral premammillary nucleus' | 0.01126 | 0.01673 | 0.01799 | 0.01082 | 0.02042 | 0.01211 | 0.00168 | 0.02832 | 0.01008 | 0.01269 | 0.01585 | 0.01970 | 0.00534 | 0.03258 | 0.01436 | -0.0532 | 0.6128 | 0.6172 | 0.9823 | 0.3637 | 0.3645 | 0.8627 | 1 |
| PVHd | 'Paraventricular hypothalamic nucleus, desce | 0.00418 | 0.01020 | 0.01369 | 0.00478 | 0.00479 | 0.00238 | 0.00479 | 0.01523 | 0.01259 | 0.00907 | 0.00392 | 0.01227 | 0.01963 | 0.00692 | 0.01595 | -0.1307 | 0.1708 | 0.0732 | 0.6285 | 0.0539 | 0.0141 | 0.3762 | 2 |
| VMH | 'Ventromedial hypothalamic nucleus' | 0.00460 | 0.00998 | 0.00574 | 0.00613 | 0.00752 | 0.00345 | 0.00130 | 0.01399 | 0.00717 | 0.00736 | 0.01142 | 0.00475 | 0.00417 | 0.00969 | 0.00437 | -0.0067 | 0.1052 | 0.8264 | 0.1961 | 0.0471 | 0.5731 | 0.0922 | 1 |
| PH | 'Posterior hypothalamic nucleus' | 0.00500 | 0.01043 | 0.01144 | 0.00503 | 0.00454 | 0.00382 | 0.00663 | 0.01648 | 0.01287 | 0.00754 | 0.00483 | 0.00868 | 0.01832 | 0.00312 | 0.01563 | -0.0969 | 0.2428 | 0.2911 | 0.9706 | 0.0897 | 0.1147 | 0.8233 | 2 |
| LH | 'Hypothalamic lateral zone' | 0.00797 | 0.01147 | 0.01460 | 0.00632 | 0.01044 | 0.00854 | 0.00658 | 0.01216 | 0.01728 | 0.00866 | 0.00779 | 0.01711 | 0.01645 | 0.01558 | 0.00926 | -0.0693 | 0.3853 | 0.0567 | 0.5426 | 0.1886 | 0.0177 | 0.3079 | 2 |
| ZI | 'Zona incerta' | 0.00442 | 0.00514 | 0.01197 | 0.00849 | 0.00294 | 0.00291 | 0.00334 | 0.00327 | 0.00760 | 0.00666 | 0.00305 | 0.00480 | 0.02182 | 0.00818 | 0.01309 | -0.1141 | 0.9148 | 0.2533 | 0.3021 | 0.7002 | 0.1038 | 0.1286 | 3 |
| ME | 'Median eminence' | 0.00089 | 0.00240 | 0.00298 | 0.00310 | 0.00034 | 0.00012 | 0.00001 | 0.00325 | 0.00073 | 0.00397 | 0.00166 | 0.00056 | 0.00008 | 0.00853 | 0.00273 | -0.0226 | 0.3781 | 0.6146 | 0.9593 | 0.1979 | 0.3539 | 0.7915 | 1 |
| MB-un | 'Midbrain' | 0.00797 | 0.00832 | 0.01271 | 0.00985 | 0.00902 | 0.00627 | 0.00673 | 0.00708 | 0.00735 | 0.00990 | 0.00895 | 0.01248 | 0.01516 | 0.01078 | 0.01242 | -0.0632 | 0.9452 | 0.0216 | 0.0218 | 0.7605 | 0.0092 | 0.0080 | 3 |
| MB-sen | 'Midbrain, sensory related' | 0.01225 | 0.00951 | 0.01401 | 0.01252 | 0.01330 | 0.01256 | 0.01063 | 0.00446 | 0.00466 | 0.01453 | 0.01441 | 0.01822 | 0.01526 | 0.01391 | 0.00863 | -0.0156 | 0.6546 | 0.7039 | 0.4576 | 0.3842 | 0.4322 | 0.2458 | 3 |
| SCs | 'Superior colliculus, sensory related' | 0.00293 | 0.00343 | 0.00481 | 0.00443 | 0.00249 | 0.00427 | 0.00055 | 0.00243 | 0.00106 | 0.00553 | 0.00471 | 0.00659 | 0.00675 | 0.00348 | 0.00243 | -0.0255 | 0.9309 | 0.4372 | 0.649 | 0.7284 | 0.2357 | 0.3948 | 1 |
| IC | 'Inferior colliculus' | 0.00744 | 0.00504 | 0.00784 | 0.01098 | 0.01000 | 0.00300 | 0.00577 | 0.00363 | 0.00390 | 0.00671 | 0.00592 | 0.01000 | 0.00710 | 0.00655 | 0.00772 | -0.0139 | 0.5171 | 0.978 | 0.0878 | 0.2781 | 0.8468 | 0.0399 | 3 |
| MB-mot | 'Midbrain, motor related' | 0.00277 | 0.00322 | 0.00518 | 0.00520 | 0.00209 | 0.00197 | 0.00179 | 0.00197 | 0.00203 | 0.00647 | 0.00242 | 0.00546 | 0.00730 | 0.00387 | 0.00408 | -0.0378 | 0.9394 | 0.1643 | 0.3797 | 0.7487 | 0.0776 | 0.1958 | 3 |
| SNr | 'Substantia nigra, reticular part' | 0.00330 | 0.00406 | 0.00703 | 0.00419 | 0.00206 | 0.00292 | 0.00403 | 0.00446 | 0.00532 | 0.00452 | 0.00193 | 0.00959 | 0.00854 | 0.00589 | 0.00409 | -0.0465 | 0.6898 | 0.1059 | 0.1988 | 0.4285 | 0.0325 | 0.0865 | 2 |
| VTA | 'Ventral tegmental area' | 0.01588 | 0.02282 | 0.02446 | 0.02214 | 0.01372 | 0.01406 | 0.01359 | 0.02289 | 0.02354 | 0.02026 | 0.01757 | 0.02570 | 0.02305 | 0.02007 | 0.02252 | -0.1166 | 0.1765 | 0.0559 | 0.8721 | 0.0823 | 0.0247 | 0.6323 | 3 |
| SCm | 'Superior colliculus, motor related' | 0.00683 | 0.00580 | 0.01010 | 0.01162 | 0.00759 | 0.00419 | 0.00390 | 0.00319 | 0.00311 | 0.01020 | 0.00670 | 0.00900 | 0.01185 | 0.00816 | 0.01139 | -0.0551 | 0.9109 | 0.3287 | 0.1631 | 0.6928 | 0.1553 | 0.0658 | 3 |
| PAG | 'Periaqueductal gray' | 0.00646 | 0.00484 | 0.00763 | 0.01116 | 0.00518 | 0.00674 | 0.00276 | 0.00199 | 0.00032 | 0.01464 | 0.00240 | 0.00183 | 0.01068 | 0.00188 | 0.01613 | -0.0501 | 0.9036 | 0.9529 | 0.8358 | 0.6795 | 0.7763 | 0.5833 | 3 |
| PRC | 'Precommissural nucleus' | 0.00987 | 0.01800 | 0.02155 | 0.01151 | 0.00489 | 0.01678 | 0.00632 | 0.01295 | 0.02932 | 0.01685 | 0.01289 | 0.02043 | 0.02699 | 0.02293 | 0.01584 | -0.1312 | 0.2823 | 0.0403 | 0.7293 | 0.1369 | 0.0171 | 0.4634 | 3 |
| APN | 'Anterior pretectal nucleus' | 0.00044 | 0.00071 | 0.00223 | 0.00129 | 0.00016 | 0.00014 | 0.00018 | 0.00020 | 0.00018 | 0.00183 | 0.00063 | 0.00024 | 0.00536 | 0.00021 | 0.00312 | -0.0295 | 0.8469 | 0.436 | 0.5352 | 0.5912 | 0.2104 | 0.2886 | 3 |
| MPT | 'Medial pretectal area' | 0.00971 | 0.01661 | 0.01500 | 0.02077 | 0.01386 | 0.00153 | 0.00269 | 0.00807 | 0.00866 | 0.02371 | 0.02601 | 0.02722 | 0.02059 | 0.00372 | 0.00846 | -0.0780 | 0.5826 | 0.7486 | 0.9729 | 0.3394 | 0.4852 | 0.8305 | 3 |
| SNc | 'Substantia nigra, compact part' | 0.00215 | 0.00263 | 0.00455 | 0.00224 | 0.00281 | 0.00108 | 0.00246 | 0.00248 | 0.00265 | 0.00446 | 0.00092 | 0.00531 | 0.00743 | 0.00421 | 0.00125 | -0.0317 | 0.8326 | 0.2954 | 0.4562 | 0.5777 | 0.1230 | 0.2403 | 2 |
| PPN | 'Pedunculopontine nucleus' | 0.00224 | 0.00251 | 0.00705 | 0.00464 | 0.00177 | 0.00141 | 0.00113 | 0.00142 | 0.00093 | 0.00654 | 0.00115 | 0.01054 | 0.01128 | 0.00376 | 0.00263 | -0.0679 | 0.9836 | 0.2293 | 0.2827 | 0.8687 | 0.0902 | 0.1333 | 3 |
| IF | 'Interfascicular nucleus raphe' | 0.00119 | 0.00221 | 0.00231 | 0.00144 | 0.00020 | 0.00131 | 0.00180 | 0.00420 | 0.00170 | 0.00253 | 0.00041 | 0.00198 | 0.00300 | 0.00111 | 0.00313 | -0.0186 | 0.5213 | 0.2239 | 0.9942 | 0.2824 | 0.1056 | 0.9215 | 2 |
| IPN | 'Interpeduncular nucleus' | 0.00201 | 0.00155 | 0.00160 | 0.00344 | 0.00069 | 0.00250 | 0.00143 | 0.00177 | 0.00167 | 0.00202 | 0.00073 | 0.00071 | 0.00231 | 0.00029 | 0.00311 | -0.0030 | 0.7746 | 0.8932 | 0.9965 | 0.5117 | 0.6639 | 0.9421 | 2 |
| RL | 'Rostral linear nucleus raphe' | 0.00317 | 0.00707 | 0.01023 | 0.00433 | 0.00046 | 0.00411 | 0.00376 | 0.01370 | 0.00146 | 0.01056 | 0.00256 | 0.00346 | 0.01407 | 0.00130 | 0.02209 | -0.1171 | 0.4983 | 0.4249 | 0.8486 | 0.2596 | 0.2014 | 0.5991 | 3 |
| CLI | 'Central linear nucleus raphe' | 0.00369 | 0.00449 | 0.01023 | 0.00380 | 0.00002 | 0.00672 | 0.00421 | 0.00749 | 0.00047 | 0.00980 | 0.00019 | 0.00012 | 0.01665 | 0.00087 | 0.02327 | -0.1148 | 0.9567 | 0.5711 | 0.6607 | 0.7845 | 0.3134 | 0.3960 | 3 |
| DR | 'Dorsal nucleus raphe' | 0.00474 | 0.00492 | 0.00566 | 0.00466 | 0.00079 | 0.01234 | 0.00118 | 0.00200 | 0.00000 | 0.01756 | 0.00012 | 0.00057 | 0.00854 | 0.00026 | 0.01326 | -0.0385 | 0.9993 | 0.9737 | 0.9894 | 0.9729 | 0.8332 | 0.8940 | 3 |
| P | 'Pons' | 0.00734 | 0.00620 | 0.00703 | 0.00926 | 0.00952 | 0.00497 | 0.00563 | 0.00578 | 0.00595 | 0.00590 | 0.00715 | 0.00873 | 0.00873 | 0.00597 | 0.00470 | -0.0009 | 0.6552 | 0.9783 | 0.7315 | 0.3870 | 0.8485 | 0.4612 | 3 |
| P-sen | 'Pons, sensory related' | 0.00890 | 0.00705 | 0.00744 | 0.01356 | 0.00800 | 0.00303 | 0.01099 | 0.00570 | 0.00875 | 0.00631 | 0.00745 | 0.01043 | 0.00948 | 0.00548 | 0.00438 | 0.0079 | 0.7354 | 0.8569 | 0.969 | 0.4641 | 0.6099 | 0.8187 | 3 |
| NLL | 'Nucleus of the lateral lemniscus' | 0.00120 | 0.00205 | 0.00482 | 0.00154 | 0.00178 | 0.00104 | 0.00043 | 0.00220 | 0.00190 | 0.00173 | 0.00236 | 0.00674 | 0.00472 | 0.00561 | 0.00219 | -0.0385 | 0.1202 | 0.0585 | 0.1237 | 0.0424 | 0.0117 | 0.0299 | 1 |
| P-mot | 'Pons, motor related' | 0.00715 | 0.00560 | 0.00601 | 0.01348 | 0.00549 | 0.00578 | 0.00385 | 0.00526 | 0.00377 | 0.00721 | 0.00616 | 0.00775 | 0.00945 | 0.00317 | 0.00365 | -0.0053 | 0.7867 | 0.9038 | 0.9696 | 0.5205 | 0.6809 | 0.8190 | 3 |
| P-sat | 'Pons, behavioral state related' | 0.00428 | 0.00472 | 0.00696 | 0.00940 | 0.00289 | 0.00294 | 0.00189 | 0.00449 | 0.00312 | 0.00840 | 0.00289 | 0.00424 | 0.01323 | 0.00216 | 0.00820 | -0.0588 | 0.9766 | 0.6637 | 0.7144 | 0.8429 | 0.4045 | 0.4482 | 3 |
| MY | 'Medulla' | 0.00609 | 0.00642 | 0.00532 | 0.00421 | 0.00824 | 0.00342 | 0.00849 | 0.00608 | 0.00614 | 0.00492 | 0.00853 | 0.00724 | 0.00648 | 0.00408 | 0.00350 | 0.0159 | 0.9751 | 0.8849 | 0.647 | 0.8367 | 0.6502 | 0.3903 | 3 |
| MY-sen | 'Medulla, sensory related' | 0.00628 | 0.00647 | 0.00541 | 0.01334 | 0.00524 | 0.00190 | 0.00463 | 0.00744 | 0.00615 | 0.00726 | 0.00503 | 0.00779 | 0.00843 | 0.00366 | 0.00177 | -0.0081 | 0.9968 | 0.9539 | 0.818 | 0.9420 | 0.7791 | 0.5588 | 3 |
| MY-mot | 'Medulla, motor related' | 0.00330 | 0.00248 | 0.00307 | 0.00986 | 0.00159 | 0.00029 | 0.00144 | 0.00293 | 0.00137 | 0.00321 | 0.00240 | 0.00469 | 0.00449 | 0.00230 | 0.00080 | -0.0122 | 0.931 | 0.9952 | 0.8356 | 0.7277 | 0.9284 | 0.5797 | 3 |
| MY-sat | 'Medulla, behavioral state related' | 0.00477 | 0.00930 | 0.00784 | 0.00644 | 0.00638 | 0.00251 | 0.00376 | 0.01313 | 0.00412 | 0.00798 | 0.01197 | 0.01671 | 0.00644 | 0.00818 | 0.00003 | -0.0251 | 0.222 | 0.6946 | 0.9303 | 0.0931 | 0.4230 | 0.7280 | 3 |

**Table 3.** ANOVA Tables for Regional Axon Density Comparisons**.** Related to Figures 2,4,5**.**

**Whole-Brain 2-Way ANOVA (Figures 4, 5, S6)**

| **ANOVA table** | F (DFn, DFd) | P value |
|---|---|---|
| Cell Type x Brain Region | F (278, 1251) = 3.959 | P<0.0001 |
| Cell Type | F (2, 9) = 5.690 | P=0.0253 |
| Brain Region | F (139.0, 1251) = 20.28 | P<0.0001 |

**Figure 4D: ORB Layer-Specific Innervation**

| **ANOVA table** | F (DFn, DFd) | P value |
|---|---|---|
| Layer x Cell Type | F (6, 27) = 4.225 | P=0.0040 |
| Layer | F (1.539, 13.85) = 21.45 | P=0.0001 |
| Cell Type | F (2, 9) = 39.86 | P<0.0001 |

**Figure 4D: AUDs Layer-Specific Innervation**

| **ANOVA table** | F (DFn, DFd) | P value |
|---|---|---|
| Layer x Cell Type | F (8, 36) = 1.635 | P=0.1493 |
| Layer | F (1.215, 10.93) = 7.283 | P=0.0172 |
| Cell Type | F (2, 9) = 44.48 | P<0.0001 |

**Figure 4D: TEa Layer-Specific Innervation**

| **ANOVA table** | F (DFn, DFd) | P value |
|---|---|---|
| Layer x Cell Type | F (8, 36) = 2.466 | P=0.0305 |
| Layer | F (1.324, 11.92) = 4.447 | P=0.0484 |
| Cell Type | F (2, 9) = 45.49 | P<0.0001 |

**Figure 4D: ECT/PERI Layer-Specific Innervation**

| **ANOVA table** | F (DFn, DFd) | P value |
|---|---|---|
| Layer x Cell Type | F (6, 27) = 3.490 | P=0.0110 |
| Layer | F (1.118, 10.06) = 2.843 | P=0.1205 |
| Cell Type | F (2, 9) = 27.44 | P=0.0001 |

**Figure 4D: ENT Layer-Specific Innervation**

| **ANOVA table** | F (DFn, DFd) | P value |
|---|---|---|
| Layer x Cell Type | F (8, 36) = 5.357 | P=0.0002 |
| Layer | F (2.733, 24.60) = 38.73 | P<0.0001 |
| Cell Type | F (2, 9) = 11.15 | P=0.0037 |

**Figure S2G (Distinction Score)**

**Repeated measures ANOVA summary**

| | | |
|---|---|---|
| F | 14.46 | |
| P value | <0.0001 | |
| **Multiple comparisons (Tukey's)** | Summary | Adjusted P Value |
| DeepTraCE vs untrained TRAILMAP mo | **** | <0.0001 |
| DeepTraCE vs Best Single Model | * | 0.0132 |
| DeepTraCE vs Max Probability of Models | *** | 0.0006 |
| DeepTraCE vs Sum of Models | * | 0.0211 |